1
EPR (Electron Paramagnetic Resonance) Spectroscopy of Polycrystalline Oxide Systems

Damien M. Murphy

1.1
Introduction

Electron Paramagnetic Resonance (EPR), sometimes referred to as Electron Spin Resonance (ESR), is a widely used spectroscopic technique to study paramagnetic centers on various oxide surfaces, which are frequently encountered in heterogeneous catalysis. Diamagnetic oxide materials can also be studied using suitable paramagnetic probes, including nitroxides and transition metal ions. These observable paramagnetic centers may include surface defects, inorganic or organic radicals, metal cations or supported metal complexes and clusters. Each of these paramagnetic species will produce a characteristic EPR signature with well defined spin Hamiltonian parameters. However, the magnetic properties, stability and reactivity of these centers may vary dramatically depending on the nature of the support or the measurement conditions. In some case, radicals stable on one surface may be transient on another, while variations in the EPR spectra of these radicals may be observed simply by altering the pre-treatment conditions of the support. Furthermore, the spin Hamiltonian parameters for a particular paramagnetic species may vary greatly from one support to another. A number of "external" perturbations, such as the specific location of the species on a surface, the presence of other interaction species in the catalytic system, the size of the metal particles, and so on, can alter the spin Hamiltonian parameters, resulting in a significantly modified EPR profile. Therefore one must interpret the experimental spectrum with careful consideration of these variables and where possible record the spectra under a variety of conditions to reinforce the assignment. Finally, the accurate analysis of the experimental spectrum can only be achieved by simulation and the resulting spin Hamiltonian parameters can then be compared to values obtained by theoretical treatments. All of the steps are crucial in order to derive a complete description of the electronic structure of the paramagnetic species, and the purpose of this chapter is to explain and illustrate how these analytical steps are performed in the interpretation of EPR spectra.

Metal Oxide Catalysis. Edited by S. David Jackson and Justin S. J. Hargreaves

ISBN: 978-3-527-31815-5

Most of the literature on surface paramagnetic centers since the mid-1990s has originated from studies in heterogeneous catalysis and material science. EPR has long been recognized as a powerful tool for the catalytic chemist, as the high sensitivity of the technique permits the detection of low concentrations of active sites. A number of review articles and monographs have appeared over the years specifically on EPR in catalysis, notably by Lunsford [1], Howe [2], Che [3], Giamello [4], Sojka [5] and Dyrek [6]. The applications of EPR spectroscopy to studies in catalysis and surface chemistry of metal oxides has also been treated in a number of papers [7, 8]. Selected examples illustrate the possibilities offered by EPR techniques towards a deeper understanding of catalyst preparation, the nature of the surface active sites and the types of reaction intermediate as well as details of catalytic reaction mechanisms [9, 10]. Hunger and Weitkamp [11] reviewed the subject of *in situ* spectroscopic methods, including *in situ* EPR to directly follow the evolution of paramagnetic surface intermediates in conditions extremely similar to those occurring in a real catalytic reactor, and so this area will not be covered here.

A complete description of the physics and fundamental concepts behind the EPR technique is beyond the scope of this chapter. Numerous textbooks on the subject of EPR, describing the practicalities of the technique, the fundamental theory and also the primary applications of the technique to different areas of chemistry, physics and biology, are widely available [12–17], in addition to the more specialist textbooks devoted to pulsed methods [18]. It is important to acknowledge that since 1993 there has been extensive development in the areas of pulsed techniques [18] and high-frequency EPR. High-frequency EPR provides several advantages over low-frequency techniques. For example, it offers increased resolution of g values, which is important in systems where spectral lines may not be resolved at lower fields. Additionally, high-frequency EPR has an increased absolute sensitivity making it particularly useful for studying systems where the number of paramagnetic species is inherently low. Pulsed EPR has also provided the experimentalist with additional tools to interrogate the paramagnetic system, particularly in relation to the advanced hyperfine techniques of ENDOR (Electron Nuclear Double Resonance), HYSCORE (Hyperfine Sublevel Correlation), ESEEM (Electron Spin Echo Envelope Modulation) and ELDOR (Electron Electron Double Resonance) detected NMR. In this chapter, only the basic principles of continuous wave (*cw*-) EPR will be presented, since this method is still the most widely used (primarily owing to instrumental availability) in studies of heterogeneous catalysis.

1.2 Basic Principles of EPR

1.2.1 The Electron Zeeman Interaction

The electron is a negatively charged particle which possesses orbital angular momentum as it moves around the nucleus. The electron also possesses spin

angular momentum **S** as it spins about its own axis. The magnitude of **S** is given by

$$\mathbf{S} = (h/2\pi)[S(S+1)]^{1/2} \tag{1.1}$$

where S = the spin quantum number and h = Planck's constant. By restricting the dimension to one specified direction, usually assigned the z direction, then the component of the spin angular momentum can only assume two values:

$$\mathbf{S}_z = M_S h/2\pi \tag{1.2}$$

The term M_S can have $(2S + 1)$ different values: $+S$, $(S - 1)$, $(S - 2)$ and so on. If the possible values of M_S differ by one and range from $-S$ to $+S$ then the only two possible values for M_S are $+1/2$ and $-1/2$ for a single unpaired electron.

The most important physical consequence of the electron spin is the associated magnetic moment, μ_e. This magnetic moment is directly proportional to the spin angular momentum and one may therefore write

$$\mu_e = -g_e \mu_B \mathbf{S} \tag{1.3}$$

The negative sign arises from the fact that the magnetic momentum of the electron is collinear but *antiparallel* to the spin itself. The factor $(g_e\mu_B)$ is referred to as the magnetogyric ratio and is composed of two important factors. The Bohr magneton, μ_B, is the magnetic moment for one unit of quantum mechanical angular momentum:

$$\mu_B = \frac{e\hbar}{2m_e} \tag{1.4}$$

where e is the electron charge, m_e is the electron mass and $\hbar = \frac{h}{2\pi}$. The factor, g_e, is known as the free electron g-factor with a value of 2.002 319 304 386 (one of the most accurately known physical constants). In a simple classical sense, one may view g_e as the proportionality constant between μ_e and $\mu_B S$.

This magnetic moment interacts with the applied magnetic field. In classical terms the energy of the interaction between the magnetic moment (μ) and the field (B) is described by

$$E = -\mu \cdot B \tag{1.5}$$

For a quantum mechanical system one must replace μ by the corresponding operator, giving the following simple spin Hamiltonian for a free electron in a magnetic field:

$$\hat{H} = g_e \mu_B S \cdot B \tag{1.6}$$

If the field is defined along the z direction, then the scalar product simplifies to the following Hamiltonian:

$$\hat{H} = g_e \mu_B S_z \cdot B \tag{1.7}$$

The S_z value in the above equation can then be replaced by M_S (in quantum mechanical terms the only operator in the right hand term above is S_z), giving

$$E = g_e \mu_B B M_S \tag{1.8}$$

Since $M_S = \pm 1/2$ only two energy states are available, which are degenerate in the absence of a magnetic field, but as B increases this degeneracy is lifted linearly as illustrated in Figure 1.1. The separation of the two levels can be matched to a quantum of radiation through the Bohr frequency condition:

$$\Delta E = h\nu = g\mu_B B \tag{1.9}$$

The existence of two Zeeman levels, and the possibility of inducing transitions from the lower energy level to the higher energy level is the very basis of EPR spectroscopy. The resonance experiment can be conducted in two ways; either the magnetic field is kept constant and the applied frequency varied, or the applied frequency is held constant and the magnetic field is varied. In EPR spectroscopy the latter case is usually used since it is far easier to vary the magnetic field over a wide range than to change frequency.

From Equation 1.9 it can be seen that the frequency required for the transition to occur is about 2.8 MHz per Gauss of applied field. This means that for the magnetic field usually employed in the laboratory, the radiation required belongs to the microwave region. For organic radicals the magnetic field used is in the region of 3400 Gauss and the corresponding applied frequency is in the microwave region of the electromagnetic spectrum (ν~9–10 GHz). This corresponds to a wavelength of about 3.4 cm and is known as the X-band frequency. Other commonly used (and commercially available) frequencies include L-band (ν~0.8–

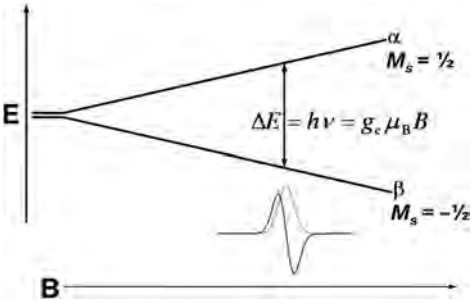

Figure 1.1 Energy levels for an electron spin ($S = \pm 1/2$) in an applied magnetic field B.

1.2 Hz), S-band (ν~3.4–3.8 Hz), K-band (ν~24 GHz), Q-band (ν~34 GHz) and W-band (ν~94 GHz). There are various advantages of going to higher and lower frequencies, depending on the paramagnetic system in question, but X-band offers the best compromise for resolution, intensity and ease of use.

It is worth noting that the SI units of magnetic field strength, or more correctly magnetic flux density, are the Tesla, T, or millitesla, mT. However for historical reasons the older units of Gauss, G, are still commonly used, where 1 mT = 10 G.

There are two fundamental differences between EPR (and NMR) and other spectroscopic techniques. Firstly, the magnetic component of the applied electromagnetic radiation (microwave) interacts with permanent magnetic moments created by the electron (or nucleus in the case of NMR). In many other spectroscopic techniques, permanent or fluctuating electric dipole moments in the sample interact with the electric field component of the electromagnetic radiation. Secondly, a distinguishing feature of EPR is the experimental setup, which is based on a monochromatic radiation source coupled with a variable magnetic field. In other words the EPR spectrum is essentially a plot of microwave absorption (at constant frequency) as a function of applied magnetic field.

At thermal equilibrium and under the influence of the external applied magnetic field, the spin population is split between the two Zeeman levels (Figure 1.1) according to the Maxwell–Boltzmann law:

$$\frac{n_1}{n_2} = e^{\frac{-\Delta E}{kT}} \tag{1.10}$$

where k is the Boltzmann constant, T the absolute temperature and n_1 and n_2 the spin populations characterized by the M_S values of +1/2 and −1/2 respectively. At 298 K in a field of about 3000 G the distribution shows that:

$$\frac{n_1}{n_2} = e^{\frac{-\Delta E}{kT}} = e^{\frac{-g_e \mu_e B}{kT}} \tag{1.11}$$

This gives a value of $n_1/n_2 = 0.9986$. The populations of the two Zeeman levels are therefore almost equal, but the slight excess in the lower level gives rise to a net absorption. However, this would very quickly lead to the disappearance of the EPR signal as the absorption of energy would equalize these two states. Consequently there has to be a mechanism for energy to be lost from the system. Such mechanisms exist and are known as relaxation processes.

1.2.2 Relaxation Processes

If electrons were to be continually promoted from a low energy level to a high level then the populations of the two energy levels would equalize and there would be no net absorption of radiation. In order to maintain a population excess in the

lower level, the odd electrons from the upper level give up the $h\nu$ quantum to return to the lower level and satisfy the Maxwell–Boltzmann law. The release of this energy occurs via a spin relaxation process, of which there are two types, known as spin–lattice relaxation and spin–spin relaxation.

In the first case, the energy is dissipated within the lattice as phonons, that is, vibrational, rotational and translational energy. The mechanism by which this dissipation occurs is known as spin–lattice relaxation. It is characterized by an exponential decay of energy as a function of time. The exponential time constant is denoted T_{1e} and is called the spin–lattice relaxation time. In the second case the initial equilibrium may also be reached by a different process. There could be an energy exchange between the spins without transfer of energy to the lattice. This phenomenon, known as spin–spin relaxation is characterized by a time constant T_{2e} called the spin–spin relaxation time.

When both spin–spin and spin–lattice relaxations contribute to the EPR line, the resonance line width (ΔB) can be written as

$$\Delta B \propto \frac{1}{T_{1e}} + \frac{1}{T_{2e}} \tag{1.12}$$

In general, $T_{1e} > T_{2e}$ and the line width depends mainly on spin–spin interactions. T_{2e} increases on decreasing the spin concentration, that is, the spin–spin distance in the system. On the other hand when T_{1e} becomes very short, below roughly 10^{-7} sec, its effect on the lifetime of a species in a given energy level makes an important contribution to the linewidth. In some cases the EPR lines are broadened beyond detection.

T_{1e} is inversely proportional to the absolute temperature ($T_{1e} \propto T^{-n}$) with n depending on the precise relaxation mechanism. In such a case, cooling the sample increases T_{1e} and usually leads to detectable lines. Thus quite often EPR experiments are performed at liquid nitrogen (77 K) or liquid helium (4 K) temperatures. On the other hand if the spin–lattice relaxation time is too long, electrons do not have time to return to the ground state. The populations of the two levels (n_1 and n_2) tend therefore to equalize and the intensity of the signal decreases, being no longer proportional to the number of spins in the sample itself. This effect, known as saturation, can be avoided by exposing the sample to low incident microwave powers. This is an important consideration, particularly when estimating the number of spins in a paramagnetic system using a reference standard (see Section 1.2.8).

1.2.3
The Nuclear Zeeman Interaction

If the interaction of the electron with an applied external magnetic field were the only effects detectable by EPR, then all spectra would consist of a single line and would be of little interest to chemists. However, the most useful chemical information that can be derived from an EPR spectrum usually results from nuclear

Table 1.1 Nuclear properties and ENDOR frequencies for selected nuclei.

Isotope	Spin (%)	Abundance	Magnetogyric ratio, $\gamma \times 10^{27}$ (J T^{-1})	ENDOR freq. (MHz at 0.350 T)
^{1}H	$\frac{1}{2}$	99.988	28.2105	14.902 18
^{2}H	1	0.011	4.3305	2.2875
^{13}C	$\frac{1}{2}$	1.07	7.0933	3.7479
^{14}N	1	99.636	2.0378	1.077 19
^{15}N	$\frac{1}{2}$	0.364	−2.8585	1.511 04
^{19}F	$\frac{1}{2}$	100	26.5396	14.016 48
^{23}Na	$\frac{3}{2}$	100	7.4620	3.944 33
^{31}P	$\frac{1}{2}$	100	11.4198	6.0380
^{39}K	$\frac{3}{2}$	93.258	1.3165	0.696 33
^{63}Cu	$\frac{3}{2}$	69.15	7.4772	3.961 56
^{65}Cu	$\frac{3}{2}$	30.85	8.010	4.2359

hyperfine structure. The source of this hyperfine structure is the interaction of magnetic nuclei, within the paramagnetic species, with the magnetic moment of the unpaired electron. Many molecules contain nuclei that have a magnetic moment, and these can interact with the electron to give hyperfine structure (Table 1.1).

Some nuclei also possess spin, when the number of neutrons and protons are both uneven, and therefore have spin angular momentum. The spin of a nucleus is described by the spin quantum number, I. The angular momentum of a nucleus with spin I is given by:

$$\text{Nuclear angular momentum } (I) = \hbar[I(I+1)]^{1/2} \tag{1.13}$$

As with electron spin angular momentum (Equation 1.1), the orientation of the vector along an axis is quantized. The magnitude of the angular momentum along the z-axis is given by $M_I h$, where M_I can have the values given by $M_I = +I$, $(I-1)$, $(I-2)$, and so on. Since nuclei possessing nuclear spin give rise to magnetic dipoles, the magnitude of this moment is given by:

$$\mu = \frac{g_n e_p h}{4\pi m_p}\sqrt{I(I+1)} \tag{1.14}$$

where g_n = the nuclear g-factor, e_p = proton charge, m_p = mass of nucleus, and the remaining symbols have their usual meaning. Since many of the terms in

Equation 1.14 are constants, they can all be replaced by another constant called the nuclear magneton μ_N:

$$\mu_N = \frac{e_p \hbar}{2m_p} \tag{1.15}$$

which has a value of $5.050 \times 10^{-29}\,\mathrm{J\,G^{-1}}$. Equation 1.14 may then be rewritten in another form:

$$\mu_N = g_N \mu_N \mathbf{I} \tag{1.16}$$

where the factor $(g_N\mu_N)$ is referred to as the nuclear magnetogyric ratio, γ_N.

Equation 1.16 is analogous to Equation 1.3 for the electron, except now the negative sign is absent since the magnetic moment of the nucleus is collinear and *parallel* to the spin itself. The simple spin Hamiltonian for a nuclear spin can thus be written

$$\hat{H} = -\gamma_N B \cdot I \tag{1.17}$$

and the eigen state values for this are:

$$E = -\gamma B M_I \tag{1.18}$$

Considering the case of a proton, which has $M_I = \pm 1/2$, then there are two spin states. In the absence of an external magnetic field the two spin states are degenerate. However, if an applied external magnetic field is applied the degeneracy is lost and two states of different energy result as shown in Figure 1.2.

In this case, the lower energy state (the α state) has both the magnetic moment and the spin parallel to the applied field. The magnetic moment of an unpaired electron can now not only interact with the external applied field, but also with local nuclear magnetic moments. It is this interaction between electron magnetic moments and nuclear magnetic moments which gives rise to hyperfine structure in the EPR spectrum.

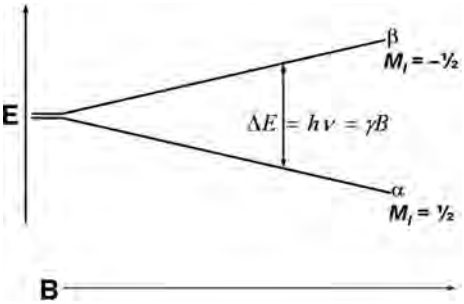

Figure 1.2 Energy levels for a nuclear spin ($I = \pm 1/2$) in an applied magnetic field $\boldsymbol{B}$ (positive γ_N).

1.2.3.1 Isotropic Hyperfine Coupling

The energy of an unpaired electron will now not only depend on the interactions of the unpaired electron (Zeeman level) and the nucleus (Nuclear Zeeman levels) with the applied external magnetic field, but also on the interaction between the unpaired electron and the magnetic nuclei. To explain how one derives the energy terms for such a system, a simple two-spin system ($S = 1/2$, $I = 1/2$) will be considered. The simplified spin Hamiltonian for this two-spin system ($S = 1/2$, $I = 1/2$) in an external applied field **B** is given as:

$$\mathrm{H} = \mathrm{H_{EZ}} - \mathrm{H_{NZ}} - \mathrm{H_{HFS}} \tag{1.19}$$

where EZ = electron Zeeman term, NZ = nuclear Zeeman term, and HFS = hyperfine interaction. This equation takes the form;

$$\hat{H} = g\mu_B B S_Z - g_N \mu_N B I_Z + hSaI \tag{1.20}$$

assuming a = the isotropic hyperfine coupling in Hertz. In the last equation it is also assumed that the g value is isotropic and the external magnetic field is aligned along the z axis. Ignoring second order terms, and in the high field approximation where the electron Zeeman interaction dominates all other interactions, the energy levels for the two-spin system ($S = 1/2$, $I = 1/2$) can be defined as:

$$E(M_S, M_I) = g\mu_B B M_S - g_N \mu_N B M_I + haM_S M_I \tag{1.21}$$

For simplicity, the electron and nuclear Zeeman energy terms can be expressed in frequency units giving:

$$E(M_S, M_I)/h = \nu_e M_S - \nu_N M_I + aM_S M_I \tag{1.22}$$

where $\nu_e = g\mu_B B/h$ and $\nu_N = g_N \mu_N B/h$. The four possible energy levels resulting from this equation (labeled E_a–E_d) can be written as follows:

$$\begin{array}{lcllll} & & & & M_S & M_I \\ E_a & = & -\frac{1}{2} g\mu_B B_o & +\frac{1}{2} g_N \mu_N B_o & +\frac{1}{4} ha & -\frac{1}{2} \quad +\frac{1}{2} \end{array} \tag{1.23a}$$

$$\begin{array}{lcllll} E_b & = & +\frac{1}{2} g\mu_B B_o & +\frac{1}{2} g_N \mu_N B_o & +\frac{1}{4} ha & +\frac{1}{2} \quad +\frac{1}{2} \end{array} \tag{1.23b}$$

$$\begin{array}{lcllll} E_c & = & +\frac{1}{2} g\mu_B B_o & -\frac{1}{2} g_N \mu_N B_o & +\frac{1}{4} ha & +\frac{1}{2} \quad -\frac{1}{2} \end{array} \tag{1.23c}$$

$$\begin{array}{lcllll} E_d & = & -\frac{1}{2} g\mu_B B_o & -\frac{1}{2} g_N \mu_N B_o & -\frac{1}{4} ha & -\frac{1}{2} \quad -\frac{1}{2} \end{array} \tag{1.23d}$$

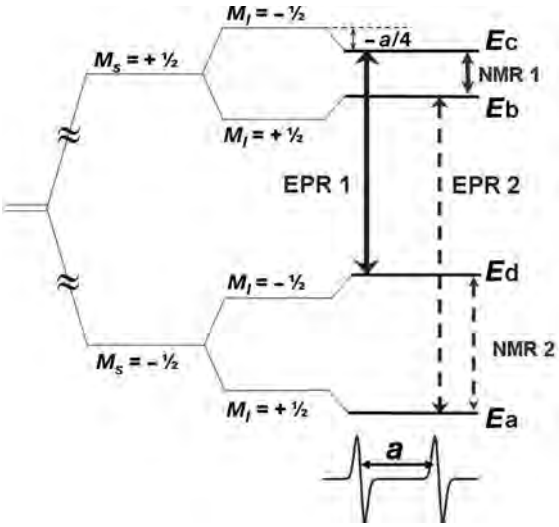

Figure 1.3 Energy level diagram for a two spin system ($S = 1/2$ and $I = 1/2$) in high magnetic field illustrating the electron Zeeman, nuclear Zeeman and hyperfine splittings. a is the isotropic hyperfine coupling with $a > 0$.

By application of the EPR selection rules ($\Delta M_I = 0$ and $\Delta M_S = \pm 1$), it is found that two possible resonance transitions can occur, namely ΔE_{cd} (labelled EPR 1) and ΔE_{ab} (labelled EPR 2), as shown in Figure 1.3:

$$\Delta E_{cd} = E_c - E_d = g\mu_B B + \frac{1}{2}ha_{iso} \tag{1.24a}$$

$$\Delta E_{ab} = E_b - E_a = g\mu_B B - \frac{1}{2}ha_{iso} \tag{1.24b}$$

These two transitions give rise to two absorption peaks at different magnetic field positions and are separated by a, the isotropic hyperfine coupling. It is possible to extract the same value of a by examination of the NMR transitions labeled 1 and 2 in Figure 1.3. These frequencies are accessed in hyperfine techniques such as ENDOR and ESEEM, and are extremely important for measuring very small hyperfine couplings, particularly in cases when a is unresolved in the EPR spectrum.

1.2.3.2 Analysis of Isotropic EPR Spectra

While most paramagnetic species encountered in heterogeneous catalysis will be associated with polycrystalline oxides, it is instructive to first examine the analysis of simple EPR spectra for systems with isotropic symmetry (found in fluid solution). When more than one equivalent nucleus is present in the system, then the energy state described by Equation 1.20 will be split by each equivalent nucleus.

Consider a paramagnet possessing two equivalent hydrogen nuclei; then, the equivalent hydrogen nuclei will split the energy states into a doublet. Since each equivalent nucleus will have the same splitting constant, the splitting by the other equivalent hydrogen will give rise to an overlap of energy levels. The interaction of an unpaired electron with n equivalent nuclei of spin I will produce $2nI + 1$ equally spaced lines. For hydrogen ($I = 1/2$) the relative intensities of the EPR absorptions are given by the binomial expansion of $(1 + x)^n$. The successive sets of coefficients for increasing n are given by Pascal's triangle.

In many cases the unpaired electron can interact with several sets of inequivalent nuclei, usually with different hyperfine couplings. In these cases interpretation of the spectra becomes very complex. Consider the case of an electron interacting with two inequivalent protons. The energy levels are split by the first proton (with coupling of a_1) and then by the second proton (with coupling a_2). Four possible transitions occur, resulting in a spectrum consisting of a "doublet of doublets" (Figure 1.4), each doublet possessing an intensity ratio of 1 : 1.

For a radical consisting of m sets of equivalent nuclei, each counting n number of equivalent nuclei, then the total number of lines is given by

$$N = (2n_1I_1 + 1)(2n_2I_2 + 1)\ldots(2n_nI_n + 1) \tag{1.25}$$

As described earlier, the number of lines in the EPR spectrum is given by the simple equation $2nI + 1$ and this holds true for n equivalent nuclei. For example, for five equivalent protons ($I = 1/2$), then $(2 \times 5 \times 1/2) + 1 = 6$ lines, producing a sextet hyperfine pattern with an intensity ratio of 1 : 5 : 10 : 10 : 5 : 1 (Table 1.2).

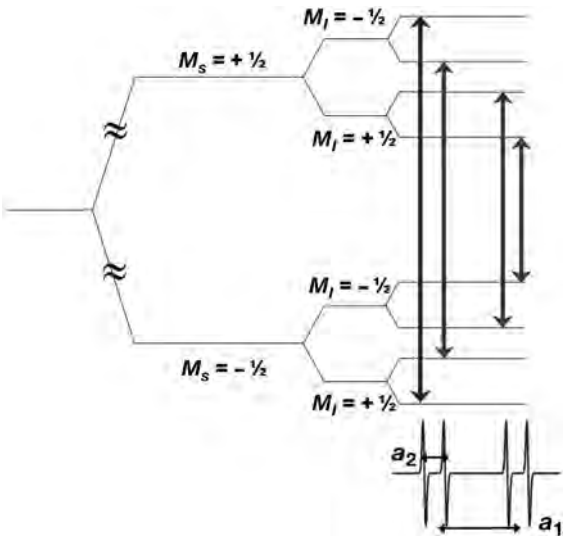

Figure 1.4 Energy level diagram for an unpaired electron ($S = 1/2$) interacting with two inequivalent $I = 1/2$ spin nuclei such that $a_1 > a_2$.

Table 1.2 Coefficients for the binominal expansion $(1 + x)^n$.

n	Pattern	Coefficients
0		1
1	Doublet	1 1
2	Triplet	1 2 1
3	Quartet	1 3 3 1
4	Pentet	1 4 6 4 1
5	Sextet	1 5 10 10 5 1
6	Septet	1 6 15 20 15 6 1
7	Octet	1 7 21 35 35 21 7 1
8	Nonet	1 8 28 56 70 56 28 8 1

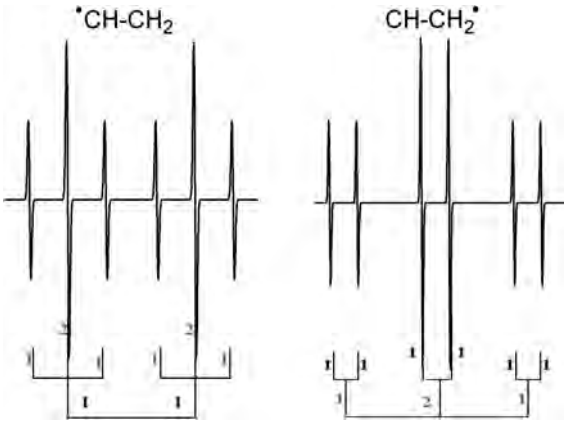

Figure 1.5 Simulated hyperfine patterns and illustrated stick diagrams for the radical fragments $^{\bullet}CHCH_2$ ($a_{CH} > a_{CH2}$) and $CH^{\bullet}CH_2$ ($a_{CH2} > a_{CH}$).

Consider the hypothetical radical fragment $^{\bullet}CH–CH_2$ which is predicted to contain six lines based on a "doublet of triplets", that is, a large doublet arising from the interaction with the CH fragment (producing two lines) and a smaller triplet due to the electron interacting more weakly with the two remote protons of the CH_2 fragment (producing three lines). The resulting stick diagram is shown in Figure 1.5. In the case where the radical is $CH–CH_2^{\bullet}$ the resulting pattern is also predicted to contain six lines, now based on a "triplet of doublets" as shown in Figure 1.5.

As the number of nuclei increases, the complexity of the spectrum rapidly increases since the spectral density depends on the number of inequivalent nuclei according to:

$$\text{Spectral density}_{\text{EPR}} = \frac{\prod_{i=1}^{k}(2N_iI_i+1)}{\sum_{i=1}^{k}2|a_i|N_iI_i} \tag{1.26}$$

This rapid increase in complexity can be illustrated by reference to the radical cation of anthracene shown in Figure 1.6. Two sets of inequivalent proton environments exist, each composed of four protons. Since the number of lines in the spectrum is given by $2nI + 1$, then the total number of predicted lines is $5 \times 5 = 25$ lines. Each group of protons is expected to produce a pentet hyperfine pattern with an intensity ratio of 1:4:6:4:1, and this pattern can indeed be identified in the spectrum (Figure 1.6). The most important point to note in the interpretation of these spectra is that the separation between the first two lines in the wings of the spectrum corresponds to the smallest hyperfine coupling (in this case a_2), regardless of how complex the pattern appears or how many lines are present. By systematically analyzing the spectrum from the outer features in to the middle features, the spectra can be finally assigned. It is common to use simulation programmes to aid in the analysis of such spectra, and, where possible, additional hyperfine techniques such as ENDOR may be used to help deconvolute the pattern. Since the spectral density in ENDOR is given by:

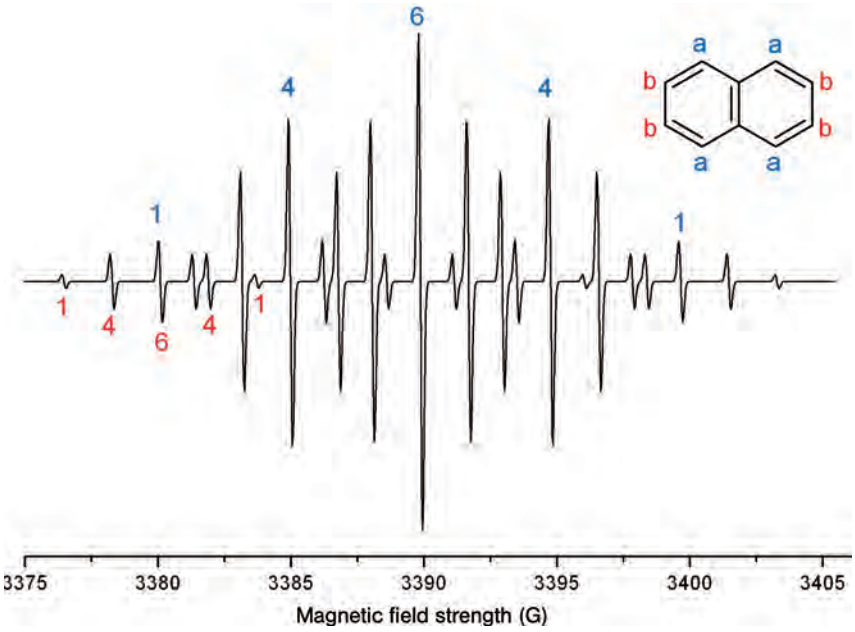

Figure 1.6 Simulated fluid solution EPR spectrum of the radical cation of anthracene. ν = 9.5 GHz, linewidth = 0.15 G, a_1 = 4.89 G, a_2 = 1.81 G.

$$\text{Spectral density}_{\text{ENDOR}} = \frac{2k}{|a_{\max}|} \tag{1.27}$$

where there are k groups of i equivalent nuclei of nuclear spin I_i and $a_{\max}$ denotes the largest hyperfine coupling constant, the resolution enhancement offered by this technique greatly simplifies the analysis.

1.2.4 The g Tensor: Origin and Significance

In Sections 1.2.1– 1.2.3, the basic theory and analysis of EPR spectra in fluid solution phase were examined. However, the theory and analysis of the spectra in the solid state, such as a heterogeneous catalyst, is more complex owing to anisotropies in the simple spin Hamiltonian introduced earlier in Equation 1.20, which only considered isotropic or averaged contributions from g and a. A more appropriate Hamiltonian for the solid state, which takes into account these anisotropies, is given by:

$$\hat{H} = \mu_B \mathbf{S}\cdot\mathbf{g}\cdot\mathbf{B} + \sum_i \left(g_N^i \mu_N^i \mathbf{I}\cdot\mathbf{B} + \mathbf{I}\cdot\mathbf{A}^i\cdot\mathbf{S}\right) \tag{1.28}$$

The isotropic g and a values are now replaced by two 3×3 matrices representing the **g** and **A** tensors and which arise from the anisotropic electron Zeeman and hyperfine interaction. Other energy terms may also be included in the spin Hamiltonian, including the anisotropic fine term **D**, for electron–electron interactions, and the anisotropic nuclear quadrupolar interaction **Q**, depending on the nucleus. Usually the quadrupolar interactions are very small, compared to A and **D**, are generally less than the inherent linewidth of the EPR signal and are therefore invisible by EPR. They are readily detected in hyperfine techniques such as ENDOR and HYSCORE. All these terms (**g, A, D**) are anisotropic in the solid state, and must therefore be defined in terms of a tensor, which will be explained in this section.

According to the basic EPR resonance Equation 1.9, the frequency required for the EPR transition depends only on **B** and μ_B since the g value in this equation is isotropic. However, since the EPR spectrum in the solid state will depend on the relative orientation of the applied field with respect to the paramagnetic species in the powder, Equation 1.9 must be modified to include this angular dependence:

$$h\nu = \mu_B g(\theta, \phi)\mathbf{B} \tag{1.29}$$

where ϕ and θ are the polar angles of the applied field within the molecular g tensor principal axis system (Figure 1.7).

Because g now depends on the angles (θ,ϕ) it should be described using the following electron Zeeman Hamiltonian:

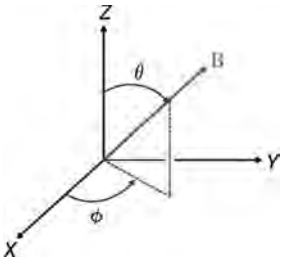

Figure 1.7 Orientation of the magnetic field with respect to the g tensor principal axis system denoted *X, Y, Z*.

$$\hat{H} = \mu_B \cdot \mathbf{S} \cdot \mathbf{g} \cdot \mathbf{B} \tag{1.30}$$

where *g* is now no longer written as a simple scalar quantity. An explicit expression for $g(\phi,\theta)$ can be found by writing the components of the field in the *g* tensor frame via the polar angles defined in Figure 1.7. For example, one must define the *g* value in terms of *B* in all three principal directions, then sum all terms to represent the anisotropic powder profile. This treatment is beyond the scope of this chapter, and can be found in any EPR textbook. However, it is sufficient to note here that the effective *g* value can finally be expressed in a form to encompass the angular terms from Equation 1.29, such that:

$$g(\theta,\phi) = \sqrt{\sin^2\theta\cdot\cos^2\phi\cdot g_1^2 + \sin^2\theta\cdot\sin^2\phi\cdot g_2^2 + \cos^2\phi\cdot g_3^2} \tag{1.31}$$

These angular variations are responsible for the different *g* values found in the EPR spectrum (i.e. qualitatively they depend on the symmetry of the electronic wave function). However these deviations from g_e actually arise from the admixture of orbital angular momentum into the spin ground state via spin orbit coupling. The extent of this admixing depends on which orbital contributes to the spin ground state (p, d or f). The real components of the **g** matrix are then given by:

$$g_{ij} = g_e\delta_{ij} + 2\lambda\sum_{m\neq 0}\frac{\langle m|l_i|n\rangle\langle n|l_j|m\rangle}{E_n - E_m} \tag{1.32}$$

where *ij* are the molecular coordinate axes, λ is the spin orbit coupling constant, E_n is the energy of the SOMO, *m* denotes the filled and empty orbitals with energy E_m, and l_i is the component of the orbital angular momentum operator. The integrals are calculated for an unpaired electron when the molecular orbitals are written as linear combinations of p or d orbitals.

What is important to note here, is the role of orbital angular momentum in the resultant EPR spectrum. For example, spin orbit coupling to empty molecular orbitals produces a negative contribution to g_{ij} while coupling to filled molecular orbitals produces a positive effect on g_{ij}. This is best illustrated with respect to

inorganic radicals, which are sometimes observed directly or indirectly in surface processes. Negative g shifts are found for $11e^{-}\pi^{*}$ diatomic radicals (such as NO, N_2^-, CO^-) compared to the expected positive g shifts for $13e^{-}\pi^{*}$ radicals (such as O_2^-). A similar effect can also be found in transition metal ions since d^1 ions are expected to produce a negative g shift (less than g_e) compared to d^9 metal ions which produce positive g shifts (due to admixture of empty versus filled molecular orbitals). Since l_z does not couple the d_{z^2} orbital to any other orbital, then according to Equation 1.32, a g_z value close to free spin is predicted for a SOMO based primarily on d_{z^2}. Therefore as a first and crude approximation, a g value close to g_e for a TMI complex can be indicative of a d_{z^2} based SOMO.

1.2.5
The A Tensor; Significance and Origin

The isotropic form of the nuclear Zeeman interaction was discussed in detail in Section 1.2.3.1. This interaction is observed in isotropic media, and also in cases where the molecular orbital hosting the unpaired electron has substantial s character. The resulting isotropic hyperfine coupling is related to the finite probability of the unpaired electron being at the nucleus. The spherical symmetry of the s orbital explains the isotropic nature of the interaction which is given by;

$$a_{iso} = \frac{8\pi}{3} g_e g_n \mu_B \mu_n |\Psi_{(0)}|^2 \tag{1.33}$$

where $|\Psi_{(0)}|^2$ is the square of the value of the wavefunction of the unpaired electron. However, for unpaired electrons associated with p, d or f orbitals, no Fermi contact occurs because of the nodes of the corresponding wavefunctions at the nucleus. The electron spin–nuclear spin interaction is therefore due to the non-spherical nature of the orbitals hosting the unpaired electron, and can be described by a classic dipolar interaction between magnetic moments. The interaction is anisotropic since it depends on the orientation of the orbital with respect to the applied field. While the isotropic interaction determines the EPR spectra of species in solution, both isotropic and anisotropic interactions can be visible in the solid state.

The interaction energy between the two magnetic moments (labelled μ_1 and μ_2) is classically given by the equation

$$E = \frac{\mu_1 \cdot \mu_2}{r^3} - \frac{3(\mu_1 \cdot \mathbf{r})(\mu_2 \cdot \mathbf{r})}{r^5} \tag{1.34}$$

where $\mathbf{r}$ is the vector relating the two magnetic moments and r is the distance between the two dipoles. The quantum mechanical analogue of Equation 1.34 is obtained by replacing the dipoles by their corresponding operators:

$$\hat{H} = -g_e \mu_B g_n \mu_n \left(\frac{I \cdot S}{r^3} - \frac{3(I \cdot \mathbf{r})(S \cdot \mathbf{r})}{r^5} \right) \tag{1.35}$$

Since the electron is not localized at one position in space, Equation 1.35 must be averaged over the electron probability distribution function. $\hat{H}$ is averaged to zero when the electron cloud is spherical (as in s orbitals) and comes to a finite value for axially symmetric orbitals. The magnitude of the anisotropic hyperfine interaction then depends on the orientation of the paramagnetic system with respect to the external field.

In the general case, both isotropic and anisotropic hyperfine interactions contribute to the experimental spectrum. The whole interaction is therefore dependent once again on orientation and must be expressed by a tensor. The effective spin Hamiltonian for this more realistic description of a paramagnetic species in the solid state was given earlier in Equation 1.28. Nevertheless the **A** tensor may be split into its component isotropic and anisotropic parts as follows;

$$A^i = \begin{bmatrix} A_1 & 0 & 0 \\ 0 & A_2 & 0 \\ 0 & 0 & A_3 \end{bmatrix} = a_{iso} + \begin{bmatrix} T_1 & 0 & 0 \\ 0 & T_2 & 0 \\ 0 & 0 & T_3 \end{bmatrix} \tag{1.36}$$

where $a_{iso} = (A_1 + A_2 + A_3)/3$. The anisotropic part of the **A** tensor corresponds to the dipolar interaction as expressed by the Hamiltonian in Equation 1.35. In a number of cases, the second term of the matrix in Equation 1.36 is a traceless tensor and has the form $(-T, -T, 2T)$. For this reason, in the case of EPR spectra of paramagnetic species having both isotropic and anisotropic hyperfine couplings and undergoing rapid tumbling in a low viscosity solution, the anisotropic term is averaged to zero and the observed hyperfine coupling corresponds to the isotropic part only. Extremely useful information can be derived from the hyperfine structure of an EPR spectrum including the s and p characters of the orbitals hosting the unpaired electron (or the coefficients of the atomic wavefunctions involved in the SOMO orbital). In simple terms this data can be deduced from the following relations;

$$C_S^2 = \frac{a_{iso}}{A_o} \quad \text{and} \quad C_P^2 = \frac{T}{B} \tag{1.37}$$

where A_o and B are the experimental, or more frequently theoretical, hyperfine couplings assuming pure s and p orbitals for the elements under consideration and coefficient $C_S^2 + C_P^2 = 1$. Appropriate corrections and orbital coefficients must be included to account for the specific orbital hosting the unpaired electron, but Equation 1.37 nevertheless illustrates simply how the spin density can be calculated to first approximation. A series of more detailed examples of these calculations will be presented in Section 1.3.

1.2.6
The D Tensor; Significance and Origin

The spin Hamiltonian described by Equation 1.28 applies to the case where a single electron ($S = 1/2$) interacts with the applied magnetic field and with

surrounding nuclei. However, it is also possible to obtain an EPR spectrum for any system containing more than one unpaired electron. If two or more electrons are present in the system ($S > 1/2$) then a new term must be added to the spin Hamiltonian to account for the interactions between the electrons. For the simplest case with two unpaired electrons the multiplicity of states can result in either a singlet ($S = 0$) or triplet ($S = 1$). Two types of interaction can result between the electrons, namely the electron-exchange interaction (i.e. the separation between the singlet and triplet states) and the electron–electron dipole interaction (i.e. the magnetic interaction between the two electrons). Only the latter interaction will be considered here.

At small distances, the two unpaired electrons will experience a strong dipole–dipole interaction analogous to the interaction between electronic and nuclear magnetic dipoles, and this gives rise to anisotropic hyperfine interactions. The electron-electron interaction is described by the spin–spin Hamiltonian given by:

$$\hat{H}_{SS} = S \cdot D \cdot S \tag{1.38}$$

where **D** is a second rank tensor (the zero field parameter) with a trace of zero. As with the **g** and **A** tensors, the **D** tensor can also be diagonalized so that $D_{xx} + D_{yy} + D_{zz} = 0$. Equation 1.38 can be added to Equation 1.30 to obtain the correct spin Hamiltonian for an $S > 1/2$ system:

$$\hat{H} = \mu_B \cdot \mathbf{S} \cdot \mathbf{g} \cdot \mathbf{B} + S \cdot D \cdot S \tag{1.39}$$

Since the trace of **D** is zero, calculation of the energy state for a system with $S = 1$ requires only two independent parameters, which are designated D and E. The spin coupling is direct in the case of organic molecules in the triplet state and biradicals, but occurs through the orbital angular momentum in the case of transition metal ions. In the latter case, the D and E terms depend on the symmetry of the crystal field acting on the ions:

$$\hat{H} = D\left(S_z^2 - \frac{S^2}{3}\right) + E\left(S_x^2 - S_y^2\right) \tag{1.40}$$

For axially symmetric molecules, the calculated shape of the $\Delta M_S = 1$ lines are given in Figure 1.8. The separation of the outer lines is $2D'$ (where $D' = D/g\mu_B$) while that of the inner lines is D (E is zero in this case). The theoretical line shape for a randomly oriented triplet with $E \neq 0$ is also shown in Figure 1.8. The separation of the outermost lines is again $2D'$ whereas that of the intermediate and inner pairs is $D' + 3E'/2$ and $D' - 3E'/2$ respectively. As the zero-field interactions become comparable to and larger than the microwave energy, the line shape exhibits severe distortions from the simulated case in Figure 1.8.

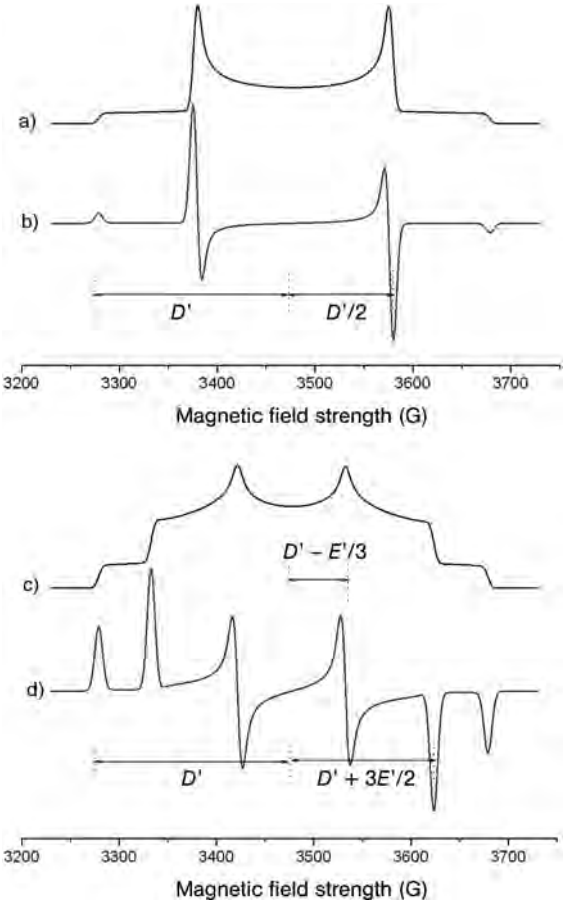

Figure 1.8 Theoretical absorption and first derivative EPR spectra of the $\Delta M_S = 1$ region of a randomly oriented triplet. Top: $S = 1$ for a given value of D ($E = 0$) and isotropic g; bottom: $S = 1$ and $D > E \neq 0$ for an isotropic g.

1.2.7
Powder EPR Spectra

Most heterogeneous catalysts are composed of numerous microcrystallites, randomly oriented in space. Therefore, unlike the more straightforward analysis of fluid solution EPR spectra (or single crystals), the interpretation of powder EPR spectra is more demanding, and often complicated by the presence of different paramagnetic active sites, distribution of **g** and **A** values, loss of spectral resolution and large line-widths. For example, different surface imperfections may create sites with different degrees of micro-heterogeneity, and if a paramagnetic species is associated with such features, then one can expect to observe complicating

features in the spectrum from **g** and **A** strain to distorted and broadened line shape. Various approaches can be adopted to unravel these complexities, and some of them will be mentioned later. However, before presenting these methods for interpreting the spectra of polycrystalline systems, it is first necessary to briefly illustrate how the *g* values of a paramagnet can be extracted from a randomly oriented solid. This analysis of the **g** tensor is generic, since the same angular dependencies also exist for the **A** and **D** tensors.

The powder spectrum of a paramagnetic species dominated by **g** anisotropy is given by the contributions of all molecules in their specific orientations with respect to the external field. The orientation of the external field with respect to the *g* principal axes was shown in Figure 1.7. All orientations will have the same probability in a polycrystalline environment, and this leads to the following equation for computing the line shape of a powder pattern:

$$\int_{-\infty}^{\infty} I(\omega)\cdot d\omega = \int_{0}^{\pi}\int_{0}^{2\pi} \sin\theta\cdot d\theta\cdot d\phi \tag{1.41}$$

According to this equation the total intensity of the EPR spectrum *(I)* is given by the sum of the contributions of each single molecular orientation in a sphere (dependent on θ and ϕ). Powder patterns are therefore usually computed numerically using a simulation program by systematic variation of the angles θ and ϕ between 0 and π and 0 and 2π respectively and weighting the spectral contributions with $\sin\theta$.

While the effective *g* value is expressed in terms of three principal values directed along three axes or directions in a single crystal, only the principal values of *g* can be extracted from the powder spectrum rather than the principal directions of the tensor with respect to the molecular axes. (Therefore it is more correct to label the observed *g* values as g_1, g_2, g_3 rather than g_{xx}, g_{yy}, g_{zz} in a powder sample.) In the simplest case, an isotropic *g* tensor can be observed, such that all three principal axes of the paramagnetic center are identical ($x = y = z$ and therefore $g_1 = g_2 = g_3$). In this case, only a single EPR line would be observed (in the absence of any hyperfine interaction). With the exception of certain point defects in oxides and the presence of signals from conduction electrons, such high symmetry cases are rarely encountered in studies of oxides and surfaces.

More commonly the symmetry of the paramagnetic centers studied in metal oxides will be lower than isotropic, such as axial ($g_{xx} = g_{yy} \neq g_{zz}$ and $A_{xx} = A_{yy} \neq A_{zz}$) rhombic ($g_{xx} \neq g_{yy} \neq g_{zz}$ and $A_{xx} \neq A_{yy} \neq A_{zz}$), monoclinic or triclinic symmetry. For example, consider a simple paramagnetic species ($S = 1/2$) with uniaxial symmetry and no hyperfine interaction. This system can be characterized by two principal axis *g* values called $g_\perp$ and $g_\parallel$. As shown earlier in Equation 1.31 for the general case where $x = y = z$, the variation in the *g* value will depend solely on the angle θ between **B** and the *x*, *y* or *z* axis. For uniaxial symmetry where $x = y \neq z$, then Equation 1.31 simplifies to:

$$B(\theta) = \frac{h\nu}{\mu_B}\left(\sqrt{g_\parallel^2\cos^2\theta + g_\perp^2\sin^2\theta}\right)^{-1} \tag{1.42}$$

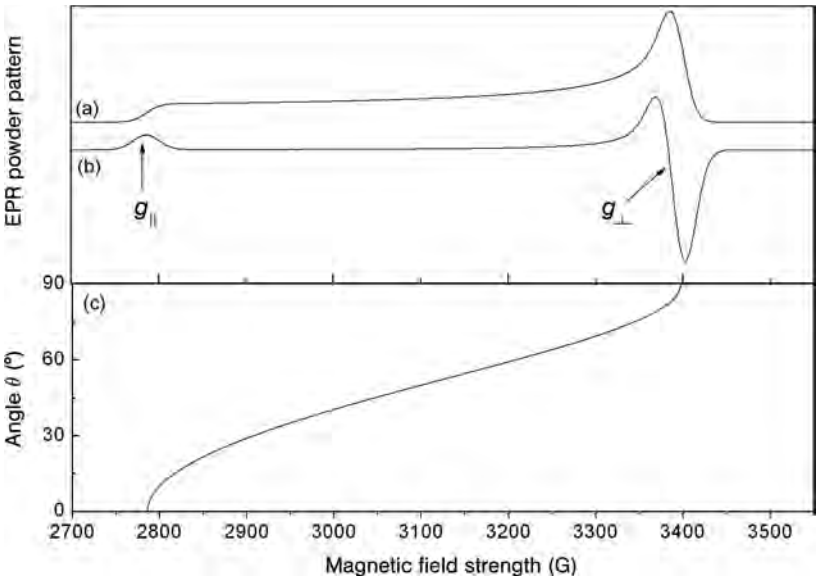

Figure 1.9 (a) Absorption and (b) first derivative EPR lineshape for a randomly oriented $S = 1/2$ spin system with axial symmetry. The angular dependence curve (θ vs field) is shown in (c).

The values of $g_{\perp}$ and $g_{||}$ therefore set the range of **B** over which absorption occurs, and two singularities will appear at the field positions $B_{||}$ and $B_{\perp}$. When the field is aligned along the unique axis ($B_{||}$), absorption occurs for those paramagnets whose field lies along the symmetry axis, corresponding to an angle of $\theta = 0°$. At this orientation only a few spins contribute to the pattern and the spectral intensity has a minimum (edge of the powder pattern) close to 2800 G. As the field moves progressively from $B_{||}$ to $B_{\perp}$, more spins come into resonance and correspondingly the intensity of the absorption line increases. At $B_{\perp}$, the absorption reaches a maximum since there is now a large plane of orientations with the field perpendicular to the symmetry axis. The *cw*-EPR spectra are always recorded as the first derivative of the absorption (Figure 1.9b), but nevertheless it is still possible to extract the values of $g_{||}$ and $g_{\perp}$ from the powder spectrum. The variation in the resonance absorption (analogous to the variation in g) as a function of the angle θ can be seen as a smooth curve with two prominent resonances at $B_{||}(g_{||})$ and $B_{\perp}(g_{\perp})$, Figure 1.9c. It is important to realize that the entire signal intensity is spread between the field positions $B_{||}$ to $B_{\perp}$ so in powder spectra with multiple sites or different paramagnetic species, the exact identification of $g_{||}$ and $g_{\perp}$ can sometimes be difficult.

In the second example, consider the case of a paramagnetic species with rhombic symmetry ($x \neq y \neq z$), characterized by three g values of g_1, g_2 and g_3. The variation in the g values now depends on the two polar angles of θ and ϕ (Equation 1.29) and a typical example of the absorption and first derivative profiles for such a

system with distinct g values is shown in Figure 1.10. Three special cases (called singularities) now occur for the resonant field positions corresponding to (i) $\theta = 0°$, (ii) $\theta = 90° = \phi$ and (iii) $\theta = 90°$, $\phi = 0°$. At $\theta = 0°$ the spins which come into resonance are those for which the applied field lies along the z axis and an absorption edge occurs producing the derivative peak corresponding to g_1. As the field moves away from the z axis, in the zy plane (such that $\phi = 90°$ and only the angle of θ varies) the resonance field position will also vary and a maximum in intensity of the absorption occurs when $\theta = 90° = \phi$ (g_2 in Figure 1.10). A similar situation occurs when the field moves from the z axis but now in the zx plane, such that all intermediate values of θ contribute to the intensity of the absorption line (since $\phi = 0°$ in this plane). The limiting point for this trend is reached when $\theta = 90°$, $\phi = 0°$ (g_3 in Figure 1.10).

The angular dependence plots illustrating the variation in the resonant field positions are thus shown in Figure 1.10c. The most intrinsic feature in the powder pattern of a rhombic $\boldsymbol{g}$ tensor consists of the fact that while only very few orientations contribute to the spectrum at $B||g_1$ and $B||g_3$ (single crystal-like case), several intermediate orientations reveal the same resonance as $B||g_2$ resulting in a maximal absorption at this field.

In the previous examples, only the $\boldsymbol{g}$ anisotropies were considered in the powder profile of the EPR spectra. In the presence of a strong hyperfine interaction (larger than the EPR linewidth), the profile of the spectrum can become even more

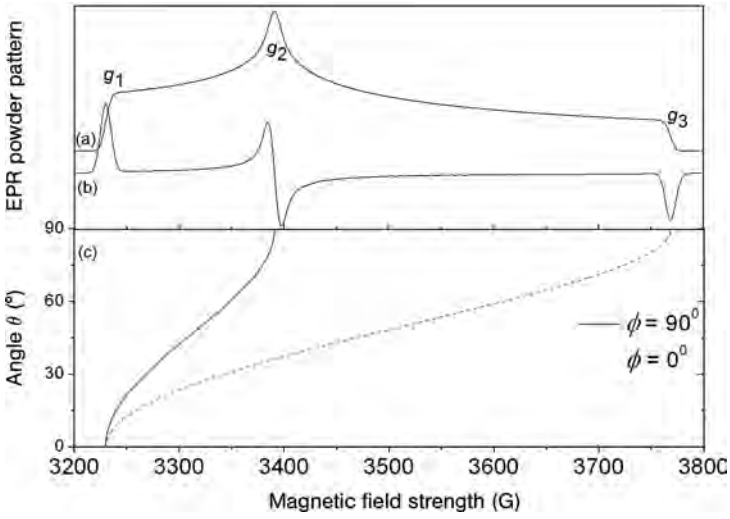

Figure 1.10 (a) Absorption and (b) first derivative EPR lineshape for a randomly oriented $S = 1/2$ spin system with rhombic symmetry ($g_1 = 2.101$, $g_2 = 2.000$, $g_3 = 1.800$, $\nu = 9.5$ GHz). The angular dependence curve (θ vs field) is shown in (c) for two angles of $\phi = 0°$ and $\phi = 90°$.

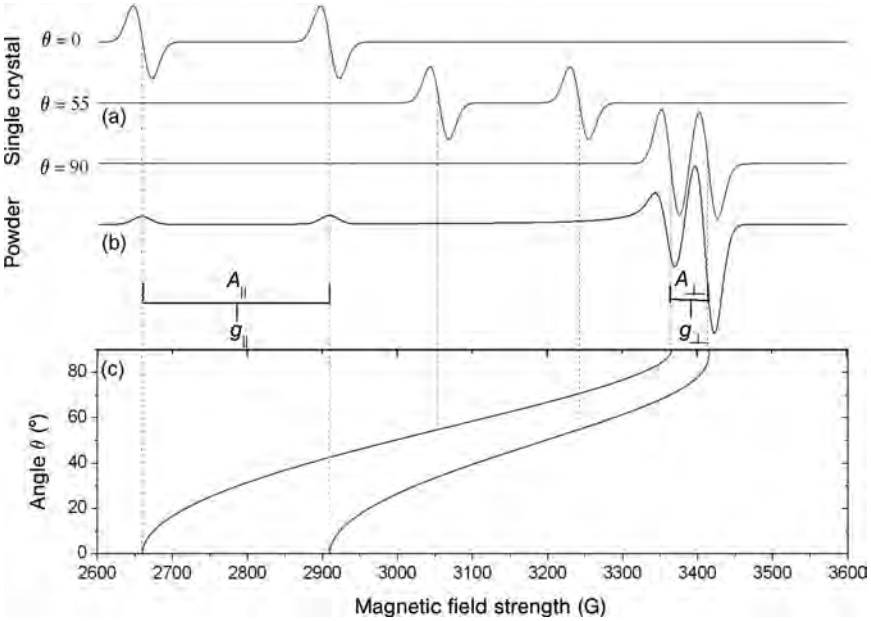

Figure 1.11 (a) Single crystal type (selected orientations of θ = 0°, 55° and 90°) and (b) first derivative powder type EPR lineshapes for a randomly oriented $S = 1/2$, $I = 1/2$ spin system with uniaxial symmetry. The angular dependence curve (θ vs field) for $m_I = \pm 1/2$ is shown in (c).

complex, particularly for large $\boldsymbol{A}$ anisotropies. Consider a simple two-spin system ($S = 1/2$ and $I = 1/2$) in a polycrystalline material, in which the overall symmetry of the paramagnetic center can be described as uniaxial. As before when the field is aligned along the unique z axis ($B_{||}$) so that θ = 0°, absorption occurs for those paramagnets whose field lies along the symmetry axis; this absorption position is defined by $g_{||}$. Owing to the interaction of the electron with the nuclear spin $I = 1/2$, the single $g_{||}$ line will now be split into a pair of lines separated by the hyperfine value $A_{||}$ (see Figure 1.11). As the field moves away from the Z axis, the resonance field position will also change. When the field is parallel to the X and Y directions ($B_{\perp}$) so that θ = 90°, absorption occurs once again as defined by the component $g_{\perp}$. This component is also split into two lines separated by the hyperfine value $A_{\perp}$. In the hypothetical single crystal case, a pair of lines would be observed for every angle of θ (three of these individual orientations are shown as an example in the upper part of Figure 1.11 corresponding to θ = 0°, 55° and 90°). In the powder spectrum, the hyperfine splittings at intermediate orientations of θ are not observed in the envelope; the splittings are only observed at the turning points or singularities corresponding to θ = 0° and 90°. Nevertheless this example demonstrates how the g and A values of $g_{\perp}$, $A_{\perp}$, $g_{||}$ and $A_{||}$ can still be extracted from the powder pattern.

1.2.8 Analysing EPR Powder Spectra; Experimental Considerations

As mentioned earlier, quite often the EPR spectra arising from a heterogeneous polycrystalline system will be complicated by a variety of factors, including the presence of several paramagnetic sites/species, g and A strain, low site symmetry, large linewidths and perhaps loss of resolved hyperfine structure. To resolve these complexities, several steps can be taken during the measurement of the spectra which may either increase spectral resolution or at least separate the components arising from other centers. These steps include measurements at variable powers and temperatures and the use of different isotopes and different frequencies. Some of the important considerations in these variables are discussed below.

1.2.8.1 Quantification of Number of Spins

The intensity of the EPR signal can of course be related to the concentration of the paramagnetic species present in the catalyst. However, although this quantitative analysis is frequently used in the literature to estimate the number of spins, it is inherently difficult to obtain absolute concentrations accurately. The relationship between signal intensity and sample concentration is given by

$$C = \frac{KI}{GP_{ij}} \tag{1.43}$$

where K is a simple proportionality constant, I is the EPR signal intensity, G the spectrometer receiver gain and P_{ij} the EPR transition probability. The proportionality constant K depends on the sample in question, and will be influenced by a variety of factors including (i) the properties of the cavity, with the sample included, (ii) the microwave power incident upon the sample and (iii) the modulation amplitude.

The intensity of the signal must be obtained in the absence of any power saturation. Since the EPR signal consists of a first derivative, rather than an absorbance, this must also be factored into the analysis. Usually double integration of the spectrum is performed over a defined scan range (after careful adjustment to the baseline). Alternatively, for a single symmetric first derivative line, the following simple relation may be used;

$$I = A_{p\text{-}p}w^2 \tag{1.44}$$

where $A_{p\text{-}p}$ is the peak to peak amplitude of the first derivative line and w is the linewidth parameter for the Lorentzian or Gaussian lineshape.

To compare the intensities of two signals (for example, between a known standard and a sample of unknown concentration), one must therefore ensure that K and P_{ij} in Equation 1.43 are identical for both sample and reference standard. In other words, factors (i)–(iii) must be identical. This is surprisingly difficult to achieve in practice, since the sample cell, sample volume, position in the cavity

and dielectric properties of sample and reference standard must be identical if factor (iii) is to be realized. In other words, the standard should ideally have identical EPR properties to that of the unknown, and must be recorded under identical instrumental conditions. Thus, for example, it would be completely inappropriate to use a DPPH reference sample as a standard to determine absolute concentration for a Cu(II)-containing catalyst.

1.2.8.2 Effects of Sample Tumbling and Rotation

In most studies of oxide surfaces, the EPR spectra will be powder-like in origin. However, in some cases, studies may be performed at the liquid–solid interface. In such circumstances, the resulting spectral profile may produce a composite profile containing both isotropic and anisotropic signals. It is rare that the spectra will be completely averaged, and frequently one may only observe distortions to the anisotropic signal (i.e. a broadening of the lines). It is therefore important to consider such effects in some detail.

Rapid tumbling, faster than the EPR timescale, of an anisotropic paramagnetic system will cause an averaging of the **g** and **A** tensors. In the hypothetical case where the tumbling is infinitely rapid compared to the EPR timescale, a fully averaged or isotropic g_{iso} and a_{iso} value will be obtained. This rarely occurs, even under ideal conditions, and in practice evidence of g and A anisotropy can still be manifested in the spectrum; specifically with respect to the linewidths of the individual lines. A good example of this partial averaging effect is shown in Figure 1.12.

This partial averaging of the signals can be easily explained by reference to the dependence of the linewidths on the value of m_I. For an $S = 1/2$ spin system, the peak-to-peak linewidths $\Delta B_{p\text{-}p}$ of the first derivative signal can be expressed as a polynominal in m_I.

$$\Delta B_{p\text{-}p} = A + Bm_I + Cm_I^2 + Dm_I^3 \tag{1.45}$$

where A, B, C and D are constants and all are positive. Usually only the first three terms on the right hand side of Equation 1.45 are considered (since D is usually very small). Clearly the linewidth depends on the value of m_I, and the m_I^2 term causes the outer lines to broaden compared to the inner lines (see Figure 1.12), although the overall shape of the spectrum still remains symmetrical at this point. Variation in the intensity across the spectrum arises from the m_I term, since transitions with the largest negative m_I value will be broadened the least, whilst transitions with the largest positive m_I value will be broadened the most. This is a very useful correlation, since it provides a means of determining the sign of a_{iso} from the spectrum if the term in m_I dominates that in m_I^2. For example, if a_{iso} is positive, the resonance at lowest field must be due to $m_I = +I$ and that at high field due to $m_I = -I$. In Figure 1.12 the reverse situation applies, therefore for ^{51}V, a_{iso} is negative, since the line at lowest field is narrower than the one at higher magnetic field.

A more qualitative way of viewing the changes to the spectra in Figure 1.12, as a function of m_I, is to consider the tumbling process as causing an averaging of

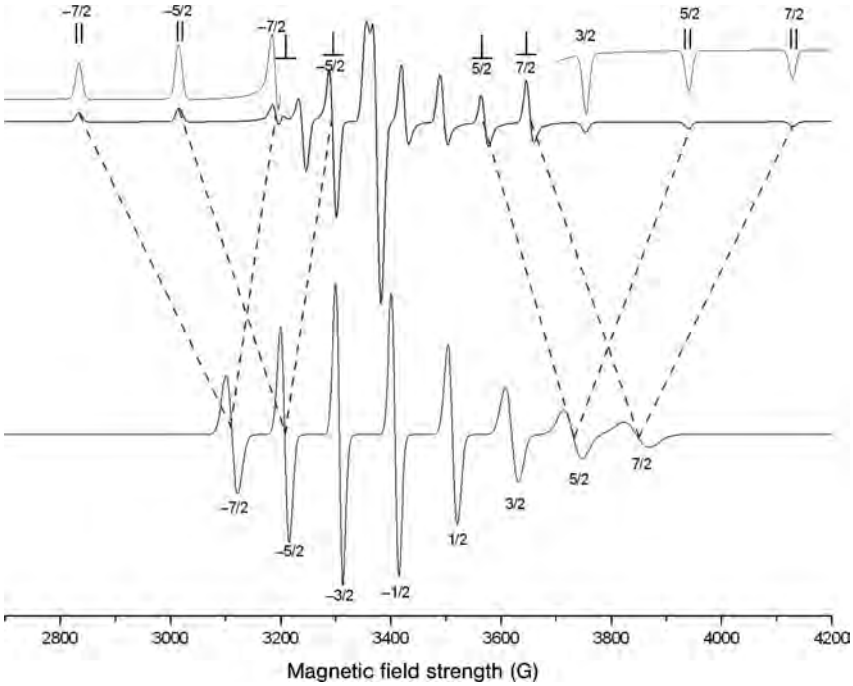

Figure 1.12 Low-temperature (rigid state) and room-temperature (mobile state) spectra of an axial VO species ($I = 7/2$) illustrating the averaging of the parallel and perpendicular hyperfine lines. The hyperfine lines are labeled with the m_I value appropriate to the particular transition.

the resonances attributable to the principal directions of the paramagnetic species. Thus each line due to one particular m_I value is averaged. The greater the difference in the magnetic field between the resonances to be averaged, the more rapidly the paramagnet must tumble in order to completely average. In other words, resonances with a particular m_I value which also have the greatest separation between them are broadened the most. In Figure 1.12, the $m_I = +7/2$ lines (in the parallel and perpendicular direction) are separated by approximately 476 Gauss, compared to the 272 Gauss separation of the two $m_I = -5/2$ lines. In the latter case the resulting line width is therefore narrower. It is therefore vitally important to be aware of partially averaged signals, and their effects on the signal linewidths, when analyzing the spectra.

1.2.8.3 **Physical State of the Sample**

In EPR spectroscopy, it is possible to measure spectra of paramagnetic samples in a variety of forms, including fluid solution, frozen solution, powdered solid or single crystal. Clearly, for heterogeneous polycrystalline systems, such as oxides, the problems of solvent choice, lossy samples, poor quality glass conditions when

frozen, and so on, are all eliminated and this facilitates the analysis of such heterogeneous systems. Polycrystalline samples do not usually present problems with respect to dielectric loss, unless they are of ionic compounds with large ionic charges or if too large a sample is placed into the cavity. With powdered solids it is important to grind the sample sufficiently to avoid any preferential orientation of the crystallites. The occurrence of preferential orientations of paramagnets in either powders or glasses may be examined by re-recording the spectrum after rotating the sample tube to give a different orientation with respect to the magnetic field. If the spectrum changes then there is some preferential orientation of the paramagnet and care must then be exercised in the interpretation of the spectrum.

1.2.8.4 **Multifrequency Measurements**

As mentioned in Section 1.2.1, EPR measurements can be performed at a range of different frequencies, and commercial spectrometers are available covering the range 1–94 GHz. Higher frequencies, including 180, 250 and 360 GHz, are also accessible in several research laboratories around the world. There are several obvious reasons for going to higher frequencies, including improved *g* resolution, improved sensitivity and simplification of spectra (particularly for systems with large zero field splittings) to name a few. Improved resolution of *g* anisotropies and small *g* value differences will undoubtedly be achieved at higher frequencies, but in some cases even moderately higher frequencies (such as K- or Q-band) may provide sufficient resolution compared to X-band, and therefore it is not necessary to make the measurements at higher field.

For example, the simulated powder profiles for a Cu(II) ion (in a square planar environment) at three different frequencies (9.5, 34 and 94 GHz) are shown in Figure 1.13. At 9.5 GHz, the *g* anisotropy is not sufficiently resolved, so that part of the parallel hyperfine component overlaps the perpendicular component. This situation complicates the analysis of the spectrum, particularly with respect to the exact determination of the *g* value, and in some cases deciding whether the spectrum is indeed axial ($g_1 \neq g_2 = g_3$) or slightly rhombic ($g_1 \neq g_2 \approx g_3$). The *g* anisotropy can be easily resolved at higher frequencies (34 or 94 GHz) but, as this example illustrates, Q-band (34 GHz) is already clearly sufficient to provide a clear assignment on exact *g* values. By comparison, the simulated powder profiles for a nitroxide spin probe are shown in Figure 1.13. At X-band frequency (9.5 GHz) the spectrum is dominated by hyperfine anisotropy with three visible lines; the *g* anisotropy is clearly very small and unresolved. At Q-band frequency the spectral resolution is clearly improved, but with a considerable degree of uncertainty in the assignment of g_1 and g_2. At W-band frequency the situation is completely resolved, and the individual *g* components can be extracted from the powder spectrum. Clearly in this particular example, W-band is essential to aid in the analysis of the spectrum. Therefore the choice of frequency largely depends on the nature of the paramagnetic center in question. Generally systems with low *g* anisotropies (small variation in *g* values) will benefit by measurements at W-band and higher frequencies.

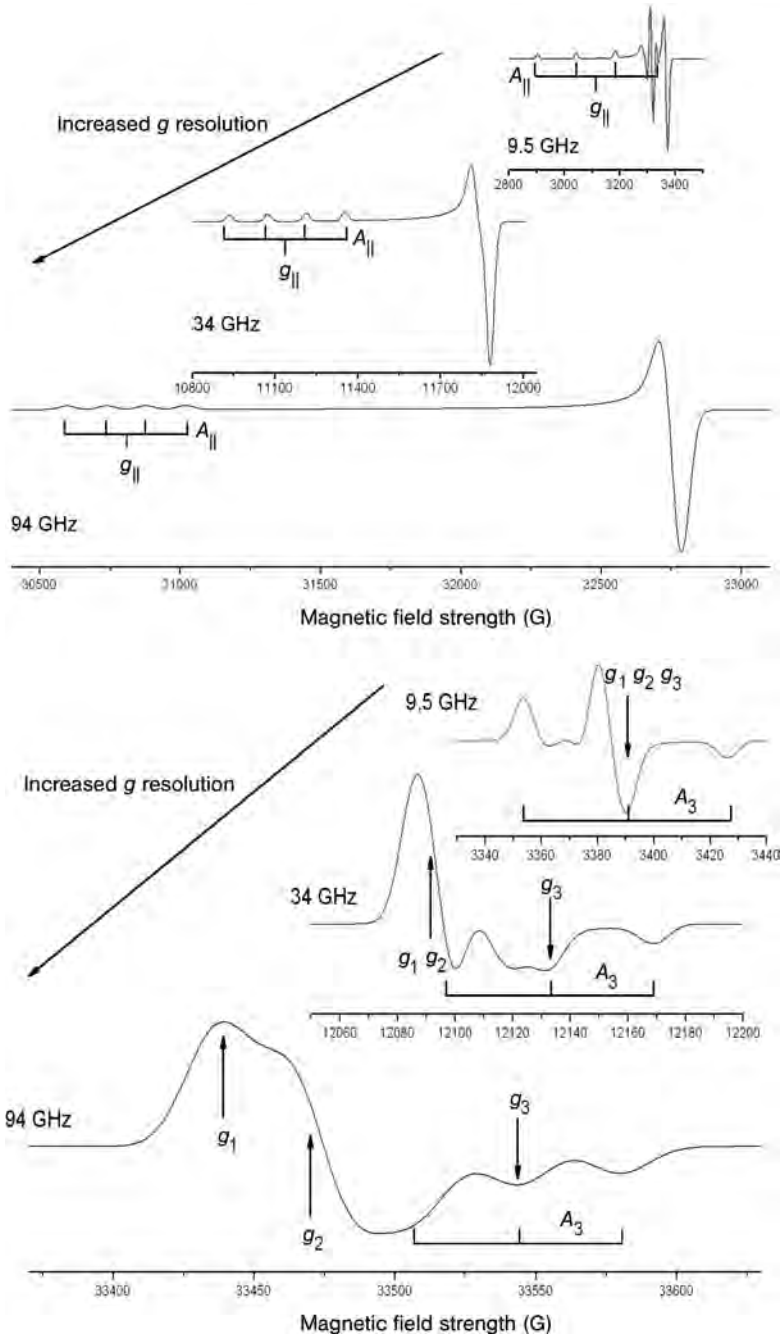

Figure 1.13 Simulated multi-frequency EPR spectra of a Cu(II) ion ($g_{\|} = 2.18$, $g_{\perp} = 2.05$, $A_{\|} = 140\,G$, $A_{\perp} = 15\,G$; upper trace) and nitroxide radical ($g_1 = 2.0084$, $g_2 = 2.006$, $g_3 = 2.002$, $A_1 = 6\,G$, $A_2 = 6\,G$, $A_3 = 36\,G$; lower trace) at X-(9.5 GHz), Q-(34 GHz) and W-(94 GHz) band freq uencies. All field units given in Gauss.

The improved sensitivity at higher field is also a strong motivation for performing high-frequency measurements. For example, depending on the width of the EPR signal, as few as 10^{11} spins can be detected at conventional X-band frequencies, whereas as few as 10^8 spins can be detected at W-band. The downside to this argument is that the sample volume also decreases dramatically at higher frequencies, so the benefits of higher sensitivity may be partially reduced. In some semiconducting oxides, the conduction electrons can produce an EPR signal, but these signals will only be observed with moderate conductivity or with small particles of materials with high conductivity. This arises because the microwave radiation that drives the spin transitions cannot penetrate deeply into highly conductive matter. Owing to the smaller microwave skin depth, high-frequency measurements will clearly benefit studies of the effect of a material's conductivity on the lineshape.

For polycrystalline samples it has also been found that partial orientation of the microcrystallites can occur in the presence of strong magnetic fields. In these circumstances, care must be taken to ensure the samples are immobilized before being brought into the magnetic field, otherwise significant distortion to the lineshape will be observed. For transition metal ion doped zeolite samples, significant g and A strain has also been observed at higher (W-band) frequency. This strain arises from the heterogeneity of the sites for the transition metal ions in the zeolite, so the resultant linewidths are considerably broadened and partially distorted.

1.2.8.5 **Variable Power and Temperature**

The applied microwave power is a very important consideration in EPR. At low values the signal amplitude will increase in direct proportion to the square root of the microwave power received by the sample in the cavity ($I \propto \sqrt{P}$). This relationship only occurs up to a certain level, beyond which the signal amplitude increases less rapidly than required by this equation, and in some cases may even start to decrease. The phenomenon whereby the rate of increase of signal amplitude is less than directly proportional to the square root of the microwave power is known as saturation. If the relationship between signal amplitude and receiver gain is important, as in the quantitative determination of spins, it is essential that non-saturating conditions are used during the measurements. At room temperature, very few transition metal ions will show saturation effects, and lower temperatures such as liquid nitrogen or liquid helium will be required to saturate the signal. By comparison, organic radicals can be easily saturated at room temperature while inorganic radicals can display saturation effects at liquid nitrogen temperatures. The different saturation characteristics for different paramagnetic species is a useful means of deconvoluting overlapping EPR signals for heterogeneous catalysts. Radical intermediates may, for example, be present simultaneously with transition metal ion active centers, but the relative contributions from the two species can be estimated by measuring the spectra at different temperatures and microwave powers.

1.2.9 A Case Study: Surface Adsorbed NO_2

As stated earlier, the amount of information available about a paramagnetic species from a powder EPR pattern is largely determined by the resolution of the spectra. If information on the $\boldsymbol{g}$ and $\boldsymbol{A}$ anisotropy can be extracted from the spectrum, then details on the electronic structure of the paramagnet can be derived. If variable temperature measurements are performed, then information on the dynamics of the species can also be derived. This can be illustrated through an example, based on the EPR spectrum of adsorbed NO_2 on an oxide surface [19].

For NO_2, the unpaired electron is mainly associated with the nonbonding orbital:

$$\psi(4a_1) = c_1N(s) + c_2N(p_z) + c_3O(p_{z1} + p_{z2}) + c_4O(p_{y1} - p_{y2}) \tag{1.46}$$

According to molecular orbital calculations, c_2 is known to be reasonably large, since the electron has substantial nitrogen p_z character. The X-band powder EPR spectrum is shown in Figure 1.14 for $^{14}NO_2$ and $^{15}NO_2$. The spectrum obtained using the ^{14}N isotope is complicated at this frequency, owing to the small $\boldsymbol{g}$ anisotropy (g_1, g_2 and g_3 are very similar to each other) and dominated by the $\boldsymbol{A}$ anisotropy. The analysis is considerably simplified using both higher frequencies (35 GHz) and the ^{15}N isotope ($I = 1/2$).

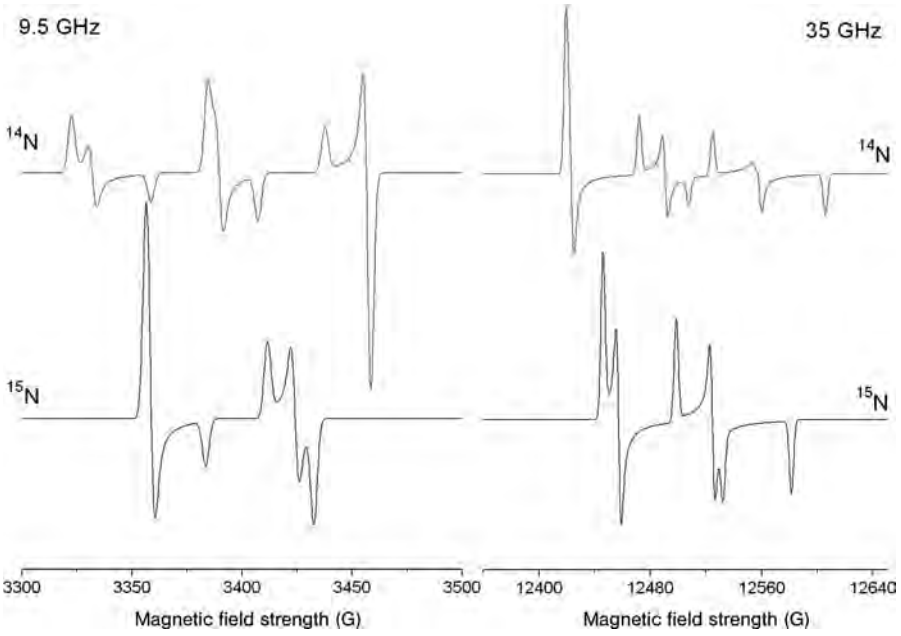

Figure 1.14 EPR spectra at X- and Q-band frequencies of surface adsorbed $^{14}NO_2$ and $^{15}NO_2$ at low temperatures.

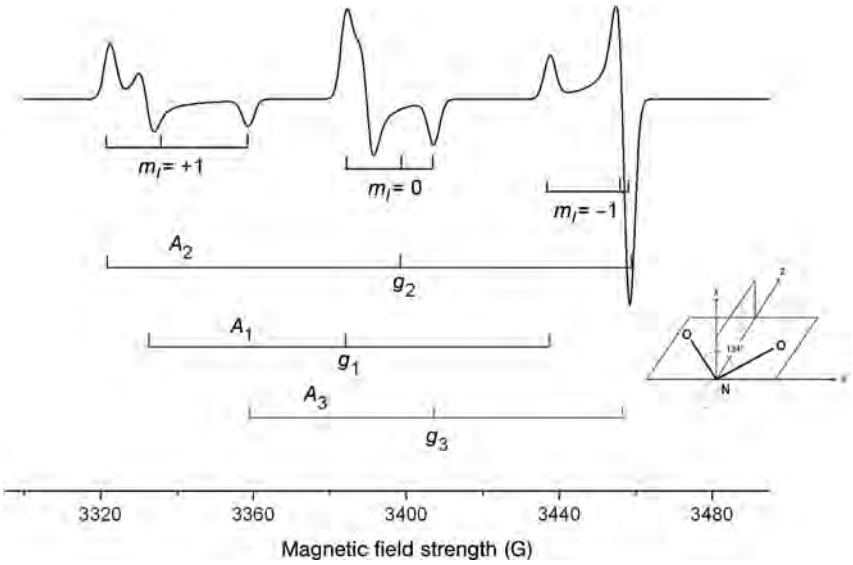

Figure 1.15 Stick diagram of the hyperfine components in the powder EPR spectrum of the randomly oriented $^{14}NO_2$ molecule. The orientation of the molecule is shown in the scheme.

For ^{14}N, the m_I values are +1, 0, −1, and therefore in the non-oriented powder pattern three components of $\boldsymbol{g}$ and $\boldsymbol{A}$ are observed for every m_I state (Figure 1.15). In the single crystal situation only three lines of equal intensity would be observed.

By analysis of the spectra in Figures 1.14 and 1.15, the spin Hamiltonian parameters can be extracted and found to be $g_1 = 2.005$, $g_2 = 2.002$, $g_3 = 1.991$, $A_1 = 52\,\text{G}$, $A_2 = 65\,\text{G}$ and $A_3 = 49\,\text{G}$. The $\boldsymbol{A}$ tensor for the ^{14}N hyperfine may thus be written as

$$A = a_{iso}I + T \tag{1.47}$$

where a_{iso} is the isotropic component (or Fermi contact term) of the hyperfine interaction and **T** is the anisotropic component. Complete analysis of the hyperfine tensor requires detailed information on the sign of the individual couplings. It is not, however, possible to determine the sign of the hyperfine coupling constants from the powder EPR spectrum. By reference to theoretical data, it is possible to determine the signs of the couplings as all positive, since other possible combinations lead to unacceptable results. The isotropic hyperfine coupling constant is also known to be 56 G, therefore only the positive sign values will give the correct value since $a_{iso} = (A_1 + A_2 + A_3)/3$. The tensor can then be broken down into its isotropic and anisotropic components as follows:

$$\begin{bmatrix} 52.7 & & \\ & 49.1 & \\ & & 67.5 \end{bmatrix} = 56.43 + \begin{bmatrix} -3.73 & & \\ & -7.33 & \\ & & 11.07 \end{bmatrix} \tag{1.48}$$

For a pure dipole interaction, the anisotropic term in the above equation should have the form $-a$, $-a$, $2a$. This implies that the unpaired electron is not purely p_z based, but also there must be some occupancy of the orthogonal p orbitals. In other words, the anisotropic tensor is actually the result of two dipolar interactions with two radius vectors, each of which is along a coordinate axis of the molecule. Therefore the anisotropic tensor is the sum of two dipolar coupling tensors and can be decomposed into two traceless components ($-a$, $-a$, $2a$) and ($-b$, $2b$, $-b$) as follows;

$$\begin{bmatrix} 52.7 & & \\ & 49.1 & \\ & & 67.5 \end{bmatrix} = 56.43 + \begin{bmatrix} -6.13 & & \\ & -6.13 & \\ & & 12.26 \end{bmatrix} + \begin{bmatrix} 2.4 & & \\ & -1.2 & \\ & & -1.2 \end{bmatrix} \tag{1.49}$$

Using the reported atomic value of the dipolar ^{14}N constant as $B_0 = \frac{4}{5} g_n \mu_n \langle r^{-3} \rangle_{2p} = 39.62\,G$, one can assess the spin density on the nitrogen 2p orbitals by direct comparison of the experimental $2a$ and $2b$ values to the atomic anisotropic constant of nitrogen using the classic formulas $\rho_{2pz} = c_{2pz^2} = 2a/B_0$ and $\rho_{2px} = c_{2px^2} = 2b/B_0$. The resultant spin densities on the nitrogen $2p_z$ and $2p_x$ orbitals are found to be 0.31 and 0.06 respectively.

The fractional occupancy of the nitrogen s orbital, may be determined from the isotropic coupling constant, which is equal to a_{iso}/A^0_{iso} (where $A^0_{iso} = 8\pi/3 g_n \mu_n \psi|(0)|^2 = 646.2\,G$ is the atomic nitrogen isotropic hyperfine constant). For $^{14}NO_2$, this gives a value of $c_1^2 = 56.43/646.2 = 0.087$. The fraction of the unpaired electron associated with the ^{14}N nucleus is then;

$$c_1^2 + c_2^2 + c_{px}^2 = 0.31 + 0.06 + 0.087 = 0.457 \tag{1.50}$$

The remaining unpaired electron will then be shared with the oxygen p_z orbitals and the surface. Information concerning the geometry of the molecule can be obtained from the hybridization ratio $\lambda^2 = c_p^2/c_s^2$. For planar molecules with C_{2v} symmetry, the dihedral angle of the molecule can be related to the hybridization ratio by $\phi = 2\cos^{-1}(\lambda^2 + 2)^{-1/2}$. Using the values of the p and s orbital occupation given above, the calculated dihedral angle is found to be 132.8°. This can be compared to the known value of 134° for the free molecule.

1.3 Example Applications in Oxide Systems

As discussed earlier, EPR is ideally suited to the study of oxide surfaces, with particular reference to heterogeneous catalysis. This subject area has been reviewed

by the author [20, 21], and the coverage was specifically devoted to paramagnetic centers present exclusively on metal oxide surfaces including S-block oxides, P-block oxides and transition metal oxides, with emphasis on the role of the surface in controlling the properties of the surface-stabilized paramagnetic species. Therefore, rather than providing an exhaustive coverage of the literature in this field, only selective examples will be presented in the following sections. The purpose of these examples is to illustrate how the fundamental concepts and experimental considerations discussed earlier are used in practice and to explore some of the limitations and advantages offered by EPR.

1.3.1 Surface Defects

Surface defects are important sites in heterogeneous catalysis, and these sites can alter the reactivity of the surface or control the anchoring of supported atoms or nanoparticles. However, these defective sites are not easily investigated by many spectroscopic techniques. While modern STM techniques can be used to detect their presence, it is far more difficult to derive useful information about their intrinsic electronic characteristics. Among the many oxides for which surface point defects have been investigated, the group II oxides have received a great deal of attention. These oxides are often used as catalysts or catalytic supports, for example in the oxidative coupling of methane (Li^+ doped MgO), isomerization and alkylation reactions (K doped MgO) or in treatments of automotive exhaust gases (CaO, BaO). Because they are also highly ionic and possess a simple lattice structure, it is no surprise that they are exploited as important model solids for investigations of the structure and reactivity of oxide surfaces in general. They are therefore widely used in surface science (single crystal faces, ultra thin oxide layers), surface chemistry (polycrystalline oxides) and quantum chemical modeling, and EPR spectroscopy has contributed significantly to the elucidation of the surface structure, particularly the surface defects.

In relation to the surface defects on the group II alkaline earth oxides, EPR has been instrumental in unraveling the electronic structure of the defects on both polycrystalline and well defined single crystal surfaces. These trapped electron centers can be formed in a number of different ways. The most convenient means on powders is by exposure of the alkaline earth oxide, such as MgO, to hydrogen atoms [22]. Spontaneous ionization of the H atoms occurs with the subsequent formation of excess electrons on the surface:

$$Mg_n^{2+}O^{2-} + H^{\bullet} \rightarrow Mg_n^{2+}(e^-)(OH^-) \tag{1.51}$$

The singly trapped electron center is paramagnetic and produces a characteristic EPR powder pattern. The electron trapping site, labeled Mg_n^{2+} in Equation 1.51, can either be a single low-coordinated cation ($n = 1$) or a small array of surface cations ($n > 1$), while the proton is stabilized by a single O^{2-} anion as a surface hydroxyl group ($O^{2-} + H^+ \rightarrow OH^-$). A typical X-band *cw*-EPR spectrum for this excess electron center on polycrystalline MgO is shown in Figure 1.16.

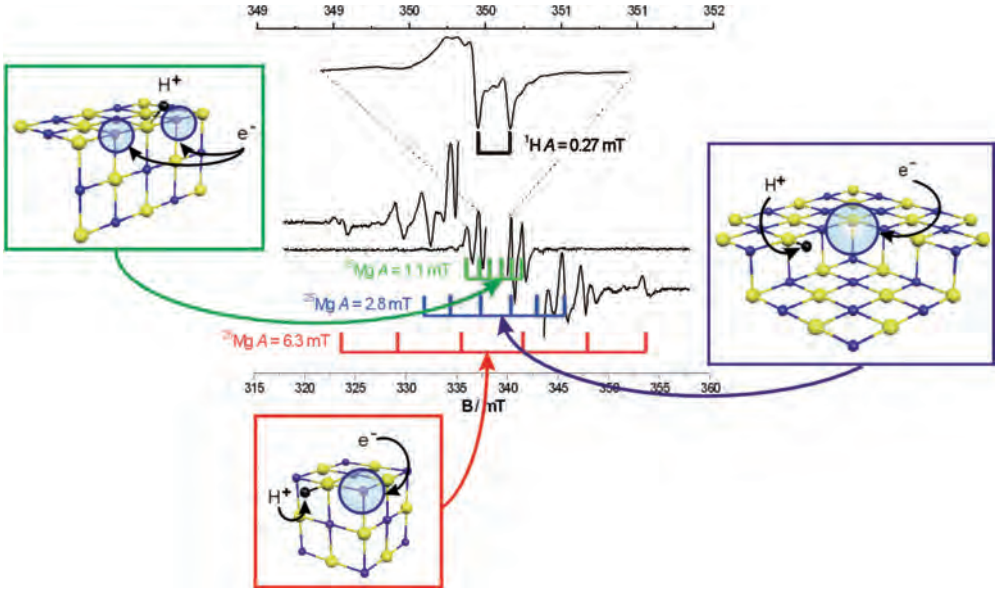

Figure 1.16 EPR spectrum and atomistic models of $(H^+)(e^-)$ centers on MgO. Reproduced from reference [22].

The powder EPR signal is dominated by a hyperfine doublet due to the interaction between the trapped electron and a single proton (^1H, $I = 1/2$). The ^1H hyperfine couplings can be more precisely determined by ENDOR, with values of $A_1 = 2.07$ G, $A_2 = 2.00$ G, $A_3 = 0.31$ G [23]. These hyperfine parameters indicate that the local symmetry of the site is lower than axial; for a purely axial system, the hyperfine parameters should take the form $A_1 = A_2 = A_\perp$ and $A_3 = A_\parallel$. Although the difference between A_1 and A_2 is small, the slightly rhombic nature of the parameters is very important and extremely informative. The magnitude of these hyperfine couplings also indicates that the electron–proton interaction is weak.

The overlap of the excess electron wave function with the charge clouds of surface ions creates further hyperfine interactions with the lattice $^{25}Mg^{2+}$ cations ($I = 5/2$ for ^{25}Mg with 10.2% natural abundance). Analysis of these ^{25}Mg hyperfine parameters proved pivotal in deriving a suitable structural model for the defect sites [24]. Three distinct ^{25}Mg hyperfine patterns can be observed (green, blue and red sextet patterns in Figure 1.16) with couplings of 11 G, 30 G and 60 G in the experimental spectrum. The magnitude of the largest hyperfine sextet (60 G) is not consistent with the traditional model of an excess electron center localized in either a bulk or surface anion vacancy, where the interaction is expected to be very weak. This large splitting was explained as arising from a large unpaired electron spin density on a single $^{25}Mg^{2+}$ cation (as opposed to being shared or distributed between an array of cations) [22]. Cluster model DFT calculations confirmed this hypothesis and revealed that the excess electrons could indeed be stabilized by the large electrostatic potential provided by a low coordinated corner or kink Mg_{3c}^{2+}

ion and a nearby proton. Both the experimentally observed EPR parameters and the energetics of the hydrogen ionization reaction, were suitably accounted for theoretically. Based on the EPR results (primarily the ^{H}A and ^{Mg}A hyperfine data) an entirely new model was proposed for the nature of the surface centers based on $(H^+)(e^-)$ electron–proton pairs, bound at morphological surface features such as a corner ion.

The remaining two ^{25}Mg hyperfine patterns (of 30 G and 11 G), could also be interpreted and explained using the new model. Theoretical calculations concluded that the 30 G hyperfine pattern was consistent with a $(H^+)(e^-)$ pair localized at the intersection of two steps. This morphological feature, also known as a reverse corner, is an important defect on polycrystalline MgO and is responsible for a number of interesting reactions, from the heterolytic dissociation of H_2 to the stabilization of alkali metal atoms. The remaining 11 G sextet pattern was more difficult to identify conclusively, since the observed parameters could equally be interpreted as arising from either the classical surface anion vacancy model, $F_s^+(H)$ center, or the $(H^+)(e^-)$ pairs model localized at surface edges and steps [25, 26]. The final assignment was eventually achieved using an MgO surface enriched with ^{17}O ($I = 5/2$). In this case, the unpaired electron produced a superhyperfine interaction with ^{17}O, and two distinct ^{17}O hyperfine sextets were identified [27]. The inequivalencies between the two ^{17}O nuclei, arose from the different spin densities created by the preferential polarization of the trapped electron towards one of the two nuclei. This polarization was created by the nearby surface OH^- group, which has the larger ^{17}O hyperfine coupling while the smaller coupling belongs to the surface O^{2-} lattice anions. This intuitive assignment was confirmed by *ab initio* calculations of the ^{17}O hyperfine tensors, which revealed that only the $(H^+)(e^-)$ pairs model, based at surface steps or edges, is consistent with the experimental data, since the ^{17}O hyperfine couplings for the $F_s^+(H)$ model were far too small.

The above example shows how very detailed information on the electronic structure of surface defect centers can be obtained by EPR even on a heterogeneous polycrystalline oxide, primarily by careful analysis of the hyperfine couplings. However, in many cases the experimental interpretations clearly benefit from complementary theoretical calculations. In this regard, EPR is the ideal partner in such interdisciplinary studies, as the spin Hamiltonian parameters provide a direct means of assessing the theoretical models by providing accurate information on spin densities. At least three different surface sites were comprehensively identified on the MgO surface, and these sites were able to spontaneously ionize H atoms and stabilize the resulting products in the form of $(H^+)(e^-)$ pairs. These $(H^+)(e^-)$ pairs can therefore be regarded as "true" color centers. The *ab initio* calculations show that the $(H^+)(e^-)$ center on MgO (reverse corner) is in fact a deep trap for the electron, which is bound by 3.71 eV and gives rise to two intense electronic transitions in the visible spectrum at 2.07 eV and 2.39 eV [25]. The same is true for corner sites [24]. This finding provides a new framework for future discussions of electron trapping since discrete morphological features, naturally present on surfaces, have been shown to act as potential wells for electron trapping without the exclusive need for surface anion vacancies.

Like the ***A*** tensor, the ***g*** tensor of the surface color centers is also very informative, but the ***g*** anisotropy is so small that it is poorly resolved at traditional X-band frequencies, particularly on a powder sample. Delicate information on the structure of paramagnetic species can however be obtained by analysis of the *g* values, but only if resolved at higher frequencies. For example, information on the point symmetry of the color center can be obtained if accurate *g* values are known. Chiesa and coworkers [28] have performed a unique multifrequency EPR study of trapped electrons on polycrystalline MgO at 9.5, 34, 190 and 285 GHz (Figure 1.17). Owing to the high fields, enhanced resolution of the Zeeman components was achieved confirming the small g anisotropies of $\Delta g_x = -0.002\,94$, $\Delta g_y = -0.002\,86$, $\Delta g_z = -0.001\,01$ with $\Delta g_i = g_i - 2.0023$. This rhombic symmetry, therefore, substantiates the assignment of the dominant surface excess electron species to $(H^+)(e^-)$ pairs (in agreement with the assignment based on analysis of the $^{H}\mathbf{A}$ tensor) bound at the surface steps or edges of the MgO powder and possessing C_{2v} symmetry [28].

Accurate determination of the ***g*** tensors at X-band frequencies can only be achieved provided that a well defined surface is available, as opposed to a polycrystalline powder, and this requires EPR measurements to be performed under ultra high vacuum (UHV) conditions on thin films or single crystals. In this case, the sample can be preferentially aligned with the laboratory magnetic field, so that a given orientation of θ is obtained. The orientational dependence of the *g* tensor can then be systematically probed, and this approach can be far more informative

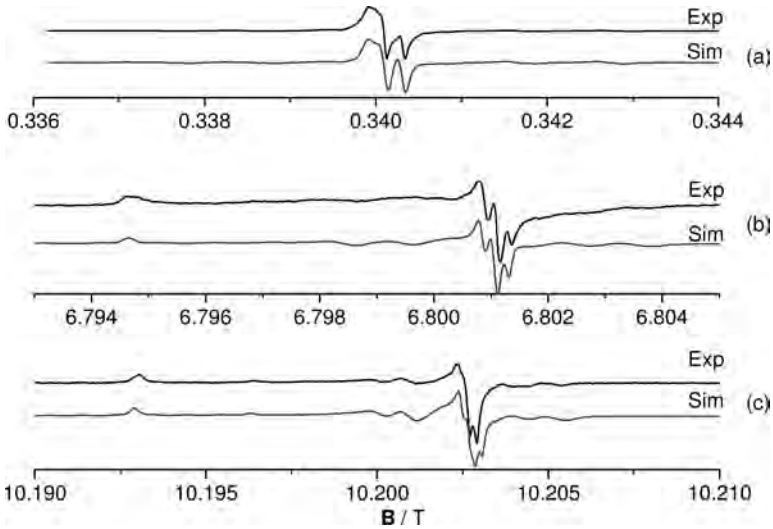

Figure 1.17 Experimental and simulated EPR spectra of $(H^+)(e^-)$ centers recorded at (a) 9.5 GHz, (b) 190 GHz and (c) 285 GHz. The high frequency spectra were obtained with a field modulation of about 0.2 G and a sweep rate of 0.001 G min^{-1}. Reproduced from reference [28].

than the summed powder pattern. Freund is the leading pioneer in the field of UHV-EPR and has shown the potential offered by EPR to the surface science community, through numerous examples ranging from defects [29–31] and adsorbates [32, 33] to model catalysts [34, 35] and supported gold atoms [36, 37]. Freund [29–31] has studied the electronic and geometric properties of trapped electron centers on thin epitaxially grown MgO(001) films on Mo(001) substrates. Idealized point symmetries of the defect sites on MgO were considered, including C_{4v} for the terrace site, C_{2v} for the edge site and C_{3v} for the corner site. For each symmetry, the components of g are dependent on the orientation of the principal g frame with respect to the laboratory reference axis frame; axial g tensors are predicted for the C_{4v} and C_{3v} symmetries whilst a rhombic symmetry is predicted for the edge site possessing C_{2v} symmetry. Rotation of the thin film by an angle θ with respect to **B**, provides information on these symmetry elements, as different components come into resonance for different angles, and these maxima in resonance absorbance will be different for an axial g tensor compared to a rhombic g tensor. The resulting spectra are shown in Figure 1.18.

The spectra were simulated based on the summed contributions from the terrace, edge and corner sites [29]. The results revealed that the g values for the edge sites were $g_{iso} = 2.0001 \pm 0.000\,05$, $\Delta g = 0.000\,40$, $\Delta B = 1.10\,\mathrm{G}$ whereas for the corner site the g values were $g_{iso} = 2.0001 \pm 0.000\,05$, $\Delta g = 0.000\,27$, $\Delta B = 1.06\,\mathrm{G}$. On the basis of the relative contributions of the two signals in the simulations and the angular dependency of the EPR lineshape, it was concluded that electron bombardment on the surface of MgO thin films leads predominantly to trapped electron centers at the edges of the MgO facets [29].

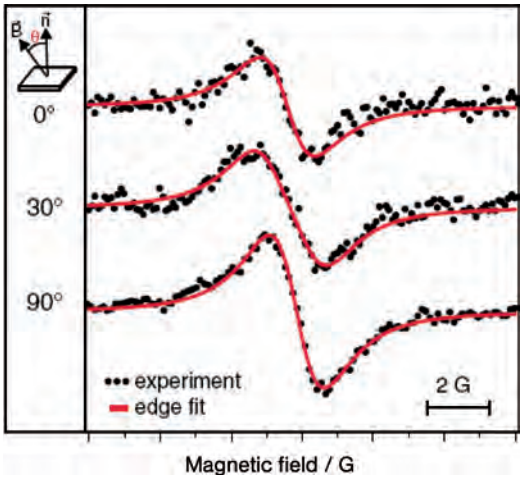

Figure 1.18 Experimental and simulated EPR spectra of color centers on 20 monolayer MgO(001)/Mo(001). Reproduced from reference [29].

1.3.2
Inorganic Radicals

The study of surface-stabilized inorganic radicals by EPR has a long history. This partially arises from their ease of generation and their favorable stability on the ionic oxide surfaces. From a catalysis point of view, such radicals are fundamentally important, since they can act as intermediates or oxidants in the catalytic cycle. If isotopic substitution of the radical is facile, then a very thorough description of the electronic and geometric properties of the species can once again be obtained by analysis of the powder EPR pattern.

In Section 1.2.9, a case study was presented on how EPR was used to identify and characterize the NO_2 radical supported on an oxide surface. To further illustrate the generic nature of this analytical approach in EPR to the investigation of the properties of surface radicals, the case of CO_2^- adsorbed on an MgO surface will be presented. This radical can be easily formed by exposure of CO_2 to MgO containing excess surface electron trapped species (that is the $(H^+)(e^-)$ centers discussed in the previous section). Although it has been studied on different oxides over the years [38, 39], a study by Chiesa and Giamello [40] demonstrates the wealth of information that can be obtained from the powder EPR spectrum. The EPR spectrum for the surface (MgO) supported $^{13}CO_2^-$ species is shown in Figure 1.19.

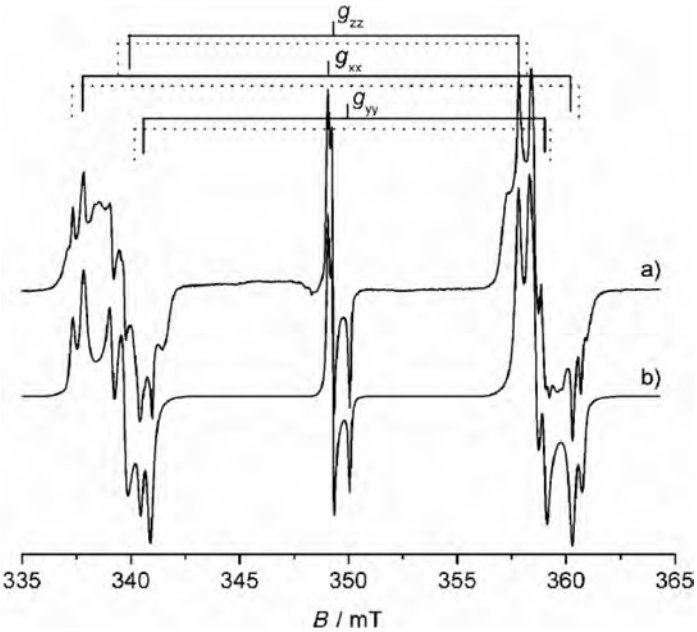

Figure 1.19 Experimental (a) and simulated (b) EPR spectrum of surface adsorbed $^{13}CO_2^-$ radicals. Reproduced from reference [40].

Simulation of the spectrum, revealed that at least two different $^{13}CO_2^-$ radicals are present (i.e. with two different sets of $\boldsymbol{g}$ and $\boldsymbol{A}$ tensors), suggesting that two different surface sites must be available for stabilizing the species. For convenience, only the spectroscopic properties of the most dominant species will be presented here. The experimental $\boldsymbol{g}$ and $\boldsymbol{A}$ tensors were found to be $g_{xx} = 2.0026$, $g_{yy} = 1.9965$, $g_{zz} = 2.0009$, $|A_{xx}| = 507.5$, $|A_{yy}| = 495.2$ and $|A_{zz}| = 629.3$ MHz. The largest deviation of the g value from $g_e = 2.002\,3$, is expected along the y axis (g_y) and is due primarily to admixture of the ground state ($4a_1$) with the first excited state ($2b_1$) while the direction of maximum hyperfine coupling coincides with the principal g value oriented along the z axis. The experimental hyperfine parameters can be decomposed into the isotropic and dipolar parts using Equation 1.47. It is necessary to know the relative signs of the hyperfine coupling for this analysis. However since a_{iso} is too large to be caused by spin polarization, it must be positive. Based on this assumption the experimental matrix can be decomposed as follows:

$$\begin{bmatrix} 507.5 & & \\ & 495.2 & \\ & & 629.3 \end{bmatrix} = 544.0 + \begin{bmatrix} -36.5 & & \\ & -48.8 & \\ & & +85.3 \end{bmatrix} \tag{1.52}$$

The large isotropic component is due to the unpaired electron spin density in the carbon 2s orbital, and this value (544 MHz) can be used to derive an estimate of the carbon 2s orbital contribution to the molecular orbital. Since the theoretical isotropic coupling constant for ^{13}C is 3777 MHz, then $c_{2s}^2 = 544/3777 = 0.144$. The anisotropic dipolar part of the hyperfine arises from unpaired spin density in the $2p_z$ orbital. However because the dipolar contribution in Equation 1.52 cannot be reduced to zero, this implies that a fraction of the spin density is allocated to the 2p orbital perpendicular to the molecular plane. Therefore, the dipolar component of Equation 1.52 must be further decomposed into two symmetrical tensors oriented along the z and x axes:

$$\begin{bmatrix} -36.5 & & \\ & -48.8 & \\ & & +85.3 \end{bmatrix} = \begin{bmatrix} -44.7 & & \\ & -44.7 & \\ & & +89.4 \end{bmatrix} + \begin{bmatrix} +8.2 & & \\ & -4.1 & \\ & & -4.1 \end{bmatrix} \tag{1.53}$$

This information may be interpreted in terms of the unpaired electron being confined to a carbon sp^2 hybrid orbital ($4a_1$) built up by carbon 2s and $2p_z$ and oxygen $2p_z$ atomic orbitals. The $2p_z$ character of the $4a_1$ molecular orbital can be estimated by comparison with the integral:

$$T_0 = 4/5 g_e \mu_B g_n \mu_n \langle 1/r^3 \rangle_{np} \tag{1.54}$$

which is the explicit expression of the dipolar interaction for the external field aligned along the symmetry axis of the $2p_z$ orbital. Since $\langle r\text{-}3 \rangle_{2p} = 5.820$ a.u.$^{-3}$, then

$c^2_{C2p_z}$ is found to be 0.416. Similarly the carbon $2p_x$ character can be determined as $c^2_{C2p_x} = 0.038$. The total electron spin density on the carbon atom is therefore $\rho^{13C} = 0.60$, leaving the remaining spin density to be shared by the oxygen atoms and the surface itself. To estimate the spin densities associated with the two oxygen atoms, one requires isotopic substitution of the radical via $C^{17}O_2^-$. The EPR spectra of $C^{17}O_2^-$ were sufficiently well resolved, that the ^{17O}A hyperfine parameters were easily identified. Analysis of the ^{17O}A tensors was carried out in a similar fashion to that described in Equations 1.47, 1.52 and 1.53 for ^{13}C, and the resultant spin density on oxygen was found to be $\rho^O(2s) = 0.019$, $\rho^O(2p_z) = 0.193$ and $\rho^O(2p_x) = -0.008$. The total spin density on the radical was therefore 1, and this elegant study demonstrates how easily this information can be obtained even from a powder EPR pattern.

Other radical species studied over polycrystalline MgO include O^- [41], O_3^- [42], CO^- [43], O_2^- [44, 45] and N_2^- [46]. For all these radical species, the most detailed information was obtained in cases which used isotopic substitution (^{17}O, ^{13}C, ^{15}N) and where the surface speciation of the radicals was minimized. If several different sites coexist for radical stabilization, then a heterogeneity of g and A values creates uncertainties in the assignments, and it may be more beneficial to sacrifice signal intensity for signal resolution. This was nicely exemplified for the N_2^- radical anion [46]. The latter radical is unusual since it is formed reversibly by low temperature physisorption of N_2 onto MgO containing the $(H^+)(e^-)$ centers [22]. At higher temperatures, the N_2 molecule desorbed from the surface regenerating the original $(H^+)(e^-)$ centers. The species was found to lie parallel to the surface and was unambiguously identified on the basis of the **g** and **A** tensors derived by careful spectral simulation of the $^{14}N_2^-$ and $^{15}N_2^-$ powder EPR patterns. The **g** tensor is typical of an 11 electron π radical with $g_{yy} > g_{xx} >> g_{zz}$ (i.e. $g_{yy} = 2.0042$, $g_{xx} = 2.0018$, $g_{zz} = 1.9719$). The z direction corresponds to the internuclear axis and the x direction is perpendicular to the surface. The hyperfine structure was found to be typical of a species with two equivalent N nuclei with $A_{xx} = 2.90\,G$, $A_{yy} = 21.50\,G$ and $A_{zz} = 4.20\,G$. Analysis of the hyperfine tensor indicated that about 90% of the total electron density is transferred from the surface to the molecule where it is mainly confined to the π^*_y orbital. *Ab initio* theoretical calculations at the DFT level indicated that a small energy barrier separates the unbound $(H^+)(e^-)/N_2$ state from the bound $(H^+)/N_2^-$ state (Figure 1.20). This result agrees with the facile reversibility of the surface-to-molecule electron transfer process. The calculated spin densities were in excellent agreement with those derived from the EPR experiments. The presence of an OH group near the adsorbed radical anion produces a detectable superhyperfine structure on the spectrum and this was also used to establish the correct orientation of the adsorbed radical on the surface [46].

In addition to the study of the $(H^+)(e^-)/N_2^-$ system, a detailed analysis of the analogous $(H^+)(e^-)/O_2^-$ complex was also reported, with particular emphasis on the ^{17}O hyperfine structure of adsorbed O_2^- [44, 45]. The Fermi contact term was evaluated as $a_{iso} = -20.3\,G$ and the resulting dipolar tensor was found to be $B_{xx} = -56\,G$, $B_{yy} = +27.5\,G$, $B_{zz} = +28.6\,G$. These values were later confirmed by

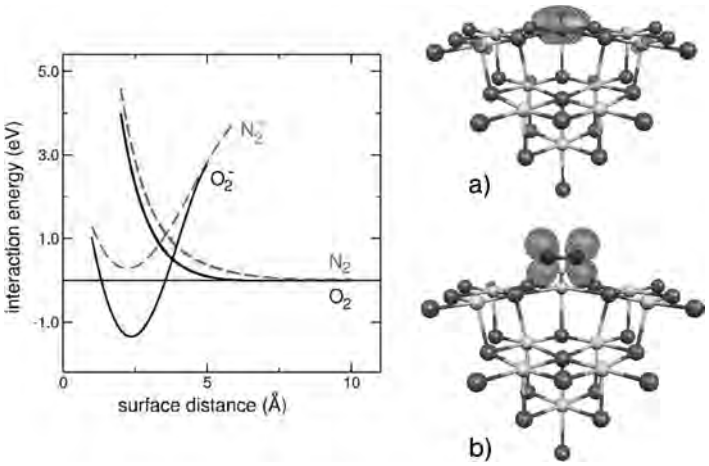

Figure 1.20 Spin density plot for (a) $(H^+)(e^-)$ centers located at a cationic reverse corner and (b) the complex formed by interaction with N_2 or O_2 molecules. On the left hand side the schematic potential energy curves for the interaction of O_2 (solid curve) and N_2 (dotted curve) molecules is shown. Negative values indicate bound states. Reproduced from reference [22].

EPR experiments. The powder spectrum contained a large number of lines and was further complicated by the presence of several off-axis extra features. These features, also known as overshoot lines, are a consequence of the relatively large anisotropy in the principal *g* values compared with substantial values of the hyperfine splitting. These features do not correspond to resonances from principal directions, and have their origins at angles in between the principal axes. They should not therefore be mistakenly interpreted as resonances from principal directions. In the $^{17}O_2^-$ case, the simulation of such a complex pattern of lines gave a_{iso} = 4.8 G and a dipolar tensor (*T*) with a value remarkably close to the theoretically calculated value. This validates the quality of the model but also the capability of modern theoretical approaches in predicting EPR hyperfine parameters. The nonreversibility of the electron transfer process from the oxide surface to the adsorbed molecule was also confirmed by theory (Figure 1.20) [22].

In one sense the radical-forming reactions between O_2 or N_2 with the electron-rich oxide surface are unusual given the low or even negative electron affinities of the two molecules (O_2 = +0.44 eV, N_2 = −2.0 eV). If the driving force for these reactions was exclusively based on the interplay between ionization energy of the surface center and molecular electron affinity, no reaction would occur. However, when electrostatic contributions between the ionic surface and the negative anions are considered, favorable reaction conditions occur. Only low-coordinated sites of the cubic crystals are capable of providing sufficiently strong stabilization energies. This fact exemplifies and highlights the importance of these low-coordinated

surface sites in the chemistry of the MgO surface over and above the rather inert Mg^{2+}_{5c} ions on the planar (100) faces.

1.3.3 Transient Radical Intermediates

Studies of transient radicals in heterogeneous catalysis have been successfully conducted by EPR using various approaches ranging from matrix isolation to spin trapping. In some cases, highly reactive species on oxide surfaces can still be investigated by traditional EPR methods by careful control of the experimental conditions such as temperature. A good example of this approach is the identification of the transient organoperoxy radicals in heterogeneous photocatalysis [47–49]. Photocatalytic oxidation of organic pollutants is frequently carried out using semiconducting polycrystalline powders such as TiO_2. On absorption of a photon, with energy equal to or greater than the band gap of TiO_2, an electron/hole pair is generated in the bulk. These charge carriers migrate towards the catalyst surface where they participate in redox reactions with the adsorbed organic molecules, and ultimately form surface radicals. In many cases, these surface (and desorbed gaseous) radical intermediates have been proposed and implicated in the photo-oxidation mechanism, particularly the oxygen-based radicals since the photocatalytic reactions are performed under aerobic conditions and molecular oxygen is an excellent electron scavenger. Despite the growing evidence for the role of active oxygen species in such reactions, surprisingly few studies have been devoted to exploring the transient intermediates by EPR.

Several EPR studies in heterogeneous photocatalysis have focused on ionic oxygen-centered radicals such as O^-, O_3^- and particularly O_2^-. However, other types of oxygen-based radicals have received far less attention, including the series of thermally unstable peroxyacyl radicals (of general formula $RCO_3^{\bullet}$) [50] and peroxy radicals (of general formula $ROO^{\bullet}$) [47–49]. A representative example of an EPR spectrum for one class of these organoperoxy radicals, is shown in Figure 1.21.

The radical is easily formed by photoirradiation of TiO_2 containing a mixture of a ketone (such as acetone or butanone) and $^{17}O_2$, at 77 K. The measurement temperature is maintained below 200 K, since the radicals are unstable at higher temperatures. After room temperature annealing, only the O_2^- radicals are observed, so it is extremely important to carefully control the experimental temperature if the transient reactive oxygen species are to be detected. The g values for the radical shown in Figure 1.21 were $g_1 = 2.035$, $g_2 = 2.008$, $g_3 = 2.002$, and these are more consistent with a peroxy radical assignment than with a purely ionic assignment (O_2^-). A definitive assignment was obtained via analysis of the ^{17}O hyperfine pattern Figure (1.21) which revealed hyperfine couplings of $^{17O}A_{||}$ (i) = 99.2 G (i.e. for $RO^{17}O^{\bullet}$) and $^{17O}A_{||}$ (ii) = 58.5 G (i.e. for $R^{17}OO^{\bullet}$) centered on the g_3 component at 2.003 [49]. This confirmed the identity of the radical as an $ROO^{\bullet}$ type species rather than $^{17}O_2^-$ for which two equivalent oxygen nuclei are expected. The unpaired spin density in peroxy radicals is known to be localized primarily in the

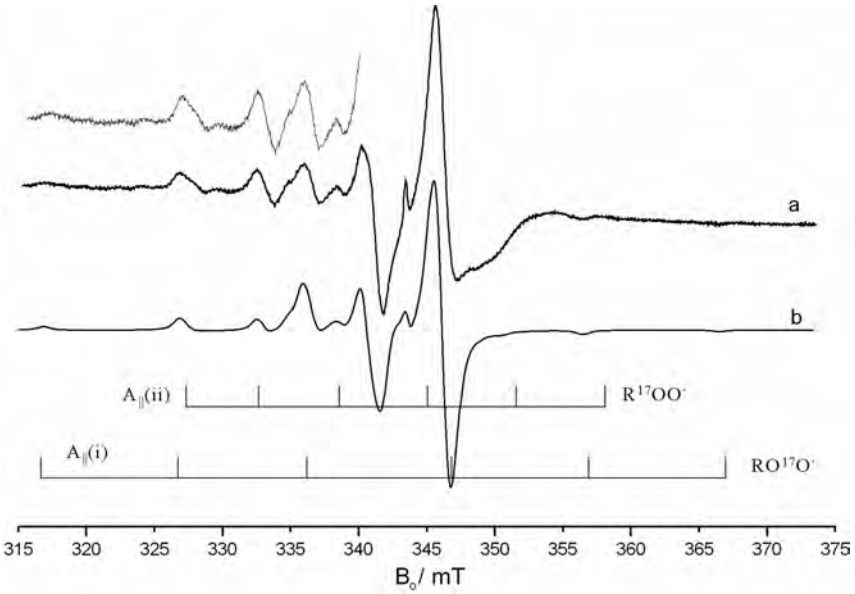

Figure 1.21 Experimental (a) and simulated (b) EPR spectrum of photoirradiated TiO_2 (at 77 K) containing coadsorbed butanone: $^{17}O_2$ in a 5 : 1 ratio (63% isotopic enrichment of ^{17}O). Reproduced from reference [49].

p_z orbitals of the two oxygen atoms, which are aligned parallel to each other, and the anisotropic hyperfine couplings arise from the spin density in the p_z orbitals which is axially symmetric, with $A_{\|} = (a + 2B)\rho$ and $A_{\perp} = (a - B)\rho$ where ρ is the spin density in the p_z orbital. An estimate of the p_z orbital spin density can be calculated using the expression $\rho(i) = |A_{\|}(i)|/\ 154\,G$, where $154\,G = |a + 2B|$. From this expression, and using the simulated hyperfine couplings, the spin density on the terminal oxygen of the butanone-derived peroxy radical was estimated to be 0.64. This falls inside the range of typical spin densities (0.61–0.70) for carbon-based peroxy radicals.

The mechanism of radical generation initially occurs via UV irradiation of the oxide producing surface trapped holes, O^-. Electron transfer from the adsorbed ketone to the surface trapped hole occurs, producing an adsorbed cation radical. This quickly deprotonates by H^+ transfer to the surface oxide, forming an intermediate radical which subsequently reacts with molecular oxygen to form the adsorbed alkylperoxy radical observable by EPR [48].

$$CH_3COCH_{3(a)} + O^-_{(s)} \rightarrow CH_3COCH^{\bullet}_{2(a)} + OH^-_{(s)} \tag{1.55}$$

$$CH_3COCH^{\bullet}_{2(a)} + O_{2(a)} \rightarrow CH_3COCH_2OO^{\bullet}_{(a)} \tag{1.56}$$

Unlike the ionic O_2^- radicals, these neutral peroxy radicals are mobile and can easily diffuse across the TiO_2 surface, undergoing further oxidative and decompo-

sition reactions. The reduced Ti^{3+}_{surf} centers are also involved in the oxidative decomposition pathways of adsorbed ketones, but via a different radical pathway [49]. Ti^{3+} involvement occurs either through the generation of stable inorganic radicals, according to Equation 1.57:

$$O_2 + Ti^{3+} \rightarrow O_2^- + Ti^{4+} \tag{1.57}$$

$$Ti^{3+} + CH_3COCH_3 \rightarrow Ti^{4+} + \{CH_3COCH_3^{\bullet -}\}^* \tag{1.58}$$

$$\{CH_3COCH_3^{\bullet -}\}^* \rightarrow CH_3^{\bullet} + CH_3CO^{\bullet} \tag{1.59}$$

or through the participation of unstable organic intermediates ($\{CH_3COCH_3^{\bullet -}\}^*$) which disproportionates to form methyl ($CH_3^{\bullet}$) and acyl ($CH_3CO^{\bullet}$) radicals (Equations 1.58–1.59). These latter radicals can be indirectly identified through their reactivity with molecular oxygen forming the corresponding organoperoxy radicals ($CH_3OO^{\bullet}$ and $CH_3CO_3^{\bullet}$) or via spin trapping. The O_2^- anions formed according to Equation 1.57 can selectively react with the adsorbed acetone (depending on the temperature) to form an associated $[\text{acetone-}O_2^-]_{(a)}$ surface complex, which can also be classified as an organoperoxy-type species [51]. This reaction can be followed by variable temperature EPR measurements, as shown in Figure 1.22.

At least three sites exist for stabilization of the O_2^- radicals on the polycrystalline TiO_2 powder, as evidenced by three different g_{zz} values of 2.019, 2.023 and 2.026.

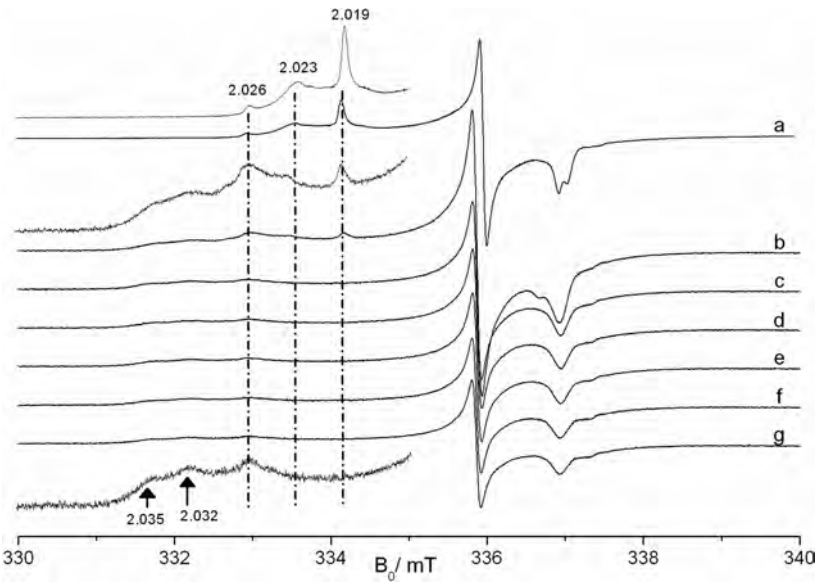

Figure 1.22 (a) EPR spectra of O_2^- radicals formed on thermally reduced TiO_2 at 140 K, and after exposure to acetone at (b) 210, (c) 212, (d) 214, (e) 216, (f) 218 and (g) 220 K. Reproduced from reference [51].

The reactivity of each O_2^- species towards acetone is not, however, the same; the species characterized by g_{zz} = 2.019 reacts first, followed by the second species with g_{zz} = 2.023. Simultaneously new signals emerge at 2.032 and 2.035. These are due to another family of organoperoxy radicals (that is the $[\text{acetone-}O_2^-]_{(a)}$ surface complex), which are thermally unstable. The most reactive O_2^- species with spin Hamiltonian parameters of g_{xx} = 2.005, g_{yy} = 2.011, g_{zz} = 2.019, $^{17O}A_{xx}$ = 7.64 mT and $A_{yy} = A_{zz}$ >1 mT, has been assigned to an oxygen radical stabilized at an anion vacancy (labeled $[\text{Vac}\ldots O_2^-]$). These results illustrate how the same nominal type of radical (O_2^-) can display differences in chemical reactivity depending on the surface site [51].

All of these radical intermediates, classified as organoperoxy species, are thermally unstable, and cannot be observed at temperatures above 250 K. This may partly explain why they have not been widely studied to date by EPR, and at least emphasizes the need to perform the experiments at low temperatures if a complete picture of the oxidative decomposition pathways in heterogeneous photocatalysis is to emerge.

1.3.4
Supported Transition Metal Ions

Transition metal oxides are versatile materials used not only as supports for catalytically active species, but also in diverse applications ranging from pigments to fuel cells to chemical sensors. In most of these applications the redox state of the transition metal ion is instrumental in controlling the final desired chemical, electrical or optical properties of the polycrystalline material or thin film. Various spectroscopic approaches are therefore required to fully characterize the nature of the "active" oxide phase, but few techniques can specifically probe, at the molecular level, the inherent properties responsible for changes in oxidation state, or distinguish the few active surface sites compared to the more abundant inactive sites. EPR is ideally suited to such investigations, primarily because it is very sensitive and also because it probes only the paramagnetic states (the redox changes) [52]. Numerous studies have appeared in recent years at the gas–solid and liquid–solid interface of TiO_2, ZrO_2, CeO_2, ZnO and various oxides of V, Cr, Fe and Cu [20, 21]. Two examples of how EPR has contributed immensely to these fields will be illustrated below.

Pitrzyk and Sojka [53] have investigated the valence and spin states of the active sites in a Co^{2+} exchanged zeolite (β and ZSM-5) during the selective catalytic reduction of nitrogen oxides with propene. Until now no clear evidence of Co^0 formation upon contact with the SCR reagents has been provided, and the existence of an intrazeolite nCo^{2+}/Co^0n couple has not been shown by EPR. Adsorption of CO at low temperature onto the Co^{2+} exchanged zeolite leads to the formation of the paramagnetic $Co^{2+}CO$ adduct characterized by the spin Hamiltonian parameters g_x = 2.234, g_y = 2.179, g_z = 2.016, $|A_x|$ = 44, $|A_y|$ = 34, $|A_z|$ = 76 G (Figure 1.23A). The spectrum was so well resolved that two other sites could be distinguished by computer simulations, illustrating nicely how sensitive the spin Hamiltonian

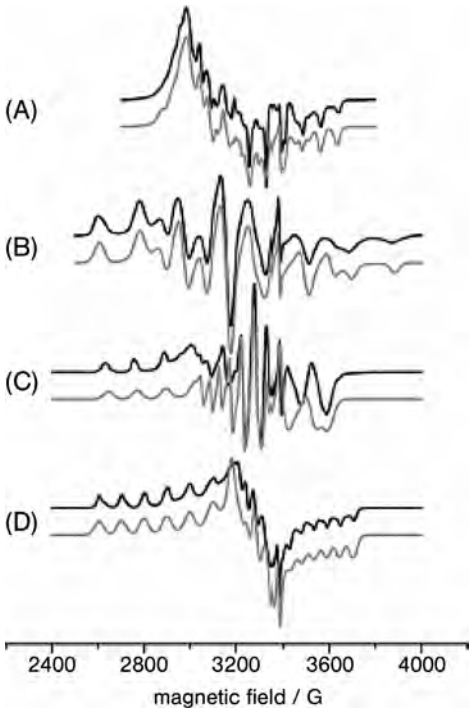

Figure 1.23 X-band experimental (black line) and simulated (grey line) EPR spectra of CoBEA sample after adsorption at 77 K of (A) 10 Torr CO, (B) 6 Torr NO, (C) 10 Torr CO after thermal decomposition (573 K in vacuum) of dinitrosyl species (spectrum B), and (D) 10 Torr propene heated at 443 K after thermal decomposition (573 K in vacuum) of dinitrosyl species (spectrum B). Reproduced from reference [53].

parameters are to their surroundings, and how informative a good simulation can be. After the sample was exposed to NO, the signal changed (Figure 1.23B). The spin Hamiltonian parameters of $g_x = 2.081$, $g_y = 2.195$, $g_z = 2.086$, $|A_x| = 182$, $|A_y| = 102$ and $|A_z| = 31$ G, were consistent with a $Co^{2+}(NO)_2$ dinitrosyl complex. Formation of this cage complex can be rationalized in terms of a spin pairing between the cobalt sites in a spin quartet state $^4Co^{2+}(d^7)$ and two NO ($^2\Pi_{1/2}$) radical ligands: $^4Co^{2+} + 2NO \rightarrow [^2Co(NO)_2]^{2+}$. The resultant spin density is largely located on the metal center ($\rho^{3d} \approx 80\%$). Thus the electronic configuration of cobalt in the dinitrosyl complex corresponds to d^9, which formally is tantamount to the zero-valent state of cobalt [53].

After formation of the dinitrosyl, the sample was evacuated at elevated temperatures and the valence state of cobalt probed again with CO. After such a treatment a new EPR signal was once again observed (Figure 1.23C) with the spin Hamiltonian parameters of $g_x = 2.199$, $g_y = 2.119$, $g_z = 1.973$, $|A_x| = 48$, $|A_y| = 125$, $|A_z| = 35$ G. These parameters are different from those of the initial carbonyl species, $Co^{2+}CO$ in Figure 1.23A, and can in fact be assigned to the Co^0CO species. This led the authors to conclude that the following simplified reaction sequence must be occurring;

$$Co^{2+} \rightarrow Co^{2+}(NO) \rightarrow Co^{0}(NO^{+}) \rightarrow Co^{0}(CO) \tag{1.60}$$

As a result, the reduction of cobalt from the divalent to the zero-valent state changes the chemistry of the system, since Co^0 readily forms complexes with hydrocarbons. This was confirmed by subsequent adsorption of propene, which produced the EPR spectrum shown in Figure 1.23D, with spin Hamiltonian parameters of $g_x = 2.096$, $g_y = 1.924$, $g_z = 2.297$, $|A_x| = 12$, $|A_y| = 52$, $|A_z| = 99$ G. This spectrum was not observed following propene exposure directly to the Co^{2+} sites.

These results highlight for the first time that at SCR temperatures the interaction of NO*x* with co-zeolites, alone or in the co-presence of propene, leads to the reduction of Co^{2+} to Co^0 via dinitrosyl intermediates [53]. The zero-valent cobalt sites generated during decomposition of the dinitrosyl species were found to exhibit enhanced affinity toward coordination of CO and propene, giving rise to the corresponding adducts with characteristic EPR spectra. The same adducts are found during SCR of NO*x* with propene, indicating that the two-electron Co^{2+}/Co^0 redox couple operates in the reaction mechanism. This study demonstrates the power of EPR to detect key intermediates, such as $Co^{2+}(NO)_2$, $Co^0(C_3H_6)_n$, and $Co^0(CO)_n$, in an important catalytic cycle.

Another surface catalytic cycle investigated by EPR has been ethene polymerization using Ziegler–Natta catalysts. Although widely studied, a detailed understanding of the reaction mechanism is far from complete largely owing to the difficulties of characterizing the extremely air-sensitive activated catalysts. Activation with a co-catalyst is usually performed using alkyl aluminum compounds such as trimethylaluminum (TMA) or triethylaluminum (TEA). A major step forward in our understanding of the mechanistic details of this reaction was recently advanced by Freund and coworkers [54, 55] using model systems consisting of an epitaxially grown $MgCl_2$ film onto which $TiCl_4$ was anchored as the active component. During activation it is believed that the Ti ions assume a lower oxidation state and when TMA is used alkyl radicals ($R^{\bullet}$) are generated:

$$TiCl_4 + AlR_3 \rightarrow RTiCl_3 + AlClR_2 \rightarrow TiCl_3 + R^{\bullet} + AlClR_2 \ (R = CH_3) \tag{1.61}$$

but until now no evidence had been presented for the existence of the alkyl radicals. The EPR spectrum of the model $TiCl_4/MgCl_2$ catalyst after activation with TMA is shown in Figure 1.24 [54]. At low $TiCl_4$ coverage the signal shown in Figure 1.24a was observed but, as the $TiCl_4$ content was increased, the intensity of the EPR signal was also found to increase (Figure 1.24b). No evidence was found for the existence of any Ti^{3+} centers, in agreement with the literature where TMA activation leads predominantly to the Ti^{2+} species.

The surface radicals observed in Figure 1.24 do not arise from the expected methyl radicals ($^{\bullet}CH_3$) for which a simple quartet structure of 1 : 3 : 3 : 1 line intensity is expected (as shown in Figure 1.23d). Instead the radical intermediates were assigned to ethyl radicals ($^{\bullet}C_2H_5$), based on comparison with the signals observed for ethyl radicals formed by irradiation of an ethyl chloride matrix at 77 K (Figure 1.24c) [54]. The radicals were shown to originate from the recombination of two methyl radicals according to

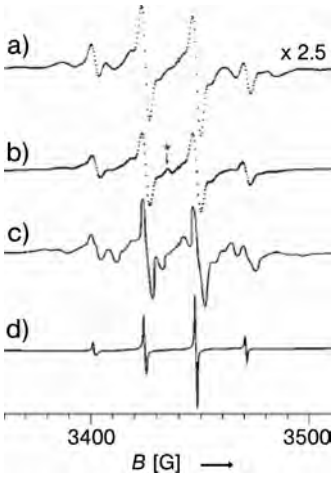

Figure 1.24 EPR spectra of alkyl radicals after (a) $AlMe_3$ adsorption at 40 K on $TiCl_4/MgCl_2$ (small Ti content), (b) $AlMe_3$ adsorption at 40 K on $TiCl_4/MgCl_2$ (higher Ti content), (c) ethyl radicals in an ethyl chloride matrix at 77 K, and (d) methyl radicals on a silica surface at 77 K. Reproduced from reference [54].

$$^{\bullet}CH_3 + Al(CH_3)_3 \rightarrow H_3C{-}^{\bullet}CH_2 + AlH(CH_3)_2 \tag{1.62}$$

The intensity of the $H_3C{-}^{\bullet}CH_2$ signal was attenuated irreversibly above 50 K and decreased below the detection limit above 80 K. This observation was explained by assuming that the ethyl radicals diffuse and recombine at these temperatures, as has been observed for other surface radicals such as $^{\bullet}CH_3$ and NO_2. These results have demonstrated for the first time how free radicals are indeed generated on the surface of an active model Ziegler–Natta catalyst.

1.4 Conclusions

Through the above series of examples, it is clear that EPR offers many advantages for the characterization of paramagnetic species on oxide surfaces. The obvious limitation of the technique is of course that it only detects paramagnetic centers. However, if paramagnetic centers, such as defects, radicals or transition metal ions, are involved in a heterogeneous process, then EPR is the ideal spectroscopic technique. To date most of the studies applied to oxides have used the traditional *cw*-EPR method. Modern pulsed techniques offer far more sensitivity and resolution than *cw*-EPR, and it is certainly hoped that these pulsed techniques will be more widely used as commercial spectrometers become more numerous in research laboratories. Compared to *cw*-EPR, the numerous hyperfine techniques

such as HYSCORE, ENDOR or ELDOR detected NMR can provide far more detailed information on the environment surrounding the local paramagnetic center, enabling a true molecular description of the active site in a heterogeneous system to be achieved. Another major development that will significantly benefit EPR studies on oxide system comes from the interaction between theory and experiment. The quantum theory of EPR parameters is now a very active field and DFT methods have significantly contributed to the interpretation of EPR spectra [56]. As some of the examples here have shown, accurate spin Hamiltonian parameters can be obtained by theory, which can guide the assignments considerably.

Acknowledgments

Dr. Emma Carter for thoroughly proofreading the manuscript and for useful comments and suggestions.

References

1 Lunsford, J.H. (1972) *Advances in Catalysis*, **22**, 265.
2 Howe, R. (1982) *Advances in Colloid and Interface Science*, **18**, 1.
3 Che, M. and Taarit, Y.B. (1985) *Advances in Colloid and Interface Science*, **23**, 235.
4 Che, M. and Giamello, E. (1987) *Studies in Surface Science and Catalysis*, **57**, B265.
5 Sojka, Z. (1995) *Catalysis Reviews–Science and Engineering*, **37**, 461.
6 Dyrek, K. and Che, M. (1997) *Chemical Reviews*, **97**, 305.
7 Sojka, Z. and Che, M. (2001) *Applied Magnetic Resonance*, **20**, 433.
8 Murphy, D.M. and Rowlands, C.C. (2001) *Current Opinion in Solid State and Materials Science*, **5**, 97.
9 Lambert, J.-F. and Che, M. (2000) *Journal of Molecular Catalysis A–Chemical*, **162**, 5.
10 Sojka, Z. (2000) *Applied Magnetic Resonance*, **18**, 71.
11 Hunger, M. and Weitkamp, J. (2001) *Angewandte Chemie–International Edition*, **40**, 2954.
12 Atkins, P.W. and Symons, M.C.R. (1967) *The Structure of Inorganic Radicals*, Elsevier, Amsterdam.
13 Ayscough, P.B. (1967) *Electron Spin Resonance*, Methuen, London.
14 Pilbrow, J.R. (1990) *Transition Ion Electron Paramagnetic Resonance*, Oxford Science Publications, Oxford.
15 Mabbs, F.E. and Collison, D. (1992) *Electron Paramagnetic Resonance of d Transition Metal Compounds (Studies in Inorganic Chemistry)*, Elsevier.
16 Atherton, N.M. (1993) *Principles of Electron Spin Resonance*, Ellis Horwood and Prentice Hall.
17 Weil, J.A., Bolton, J.R. and Wertz, J.E. (1994) *Electron Paramagnetic Resonance: Elementary Theory and Practical Applications*, John Wiley and Sons.
18 Schweiger, A. and Jeschke, G. (2001) *Principles of Pulse Electron Paramagnetic Resonance*, Oxford University Press, Oxford.
19 Lunsford, J.H. (1968) *Journal of Colloid and Interface Science*, **26**, 355.
20 Murphy, D.M. and Giamello, E. (2002) EPR of Paramagnetic Centres on Solid Surfaces, in *Electron Paramagnetic Resonance* (eds B.C. Gilbert, M.J. Davies and D.M. Murphy), Royal Society of Chemistry, Cambridge, **18**, p. 183.
21 Murphy, D.M. and Chiesa, M. (2004) EPR of Paramagnetic Centres on Solid Surfaces, in *Electron Paramagnetic Resonance* (eds. B.C. Gilbert, M.J. Davies and D.M. Murphy), Royal Society of Chemistry, Cambridge, **19**, p. 279.
22 Chiesa, M., Paginini, M.C., Giamello, E., Murphy, D.M., Di Valentin, C. and Pacchioni, G. (2006) *Accounts of Chemical Research*, **39**, 861.

23 Murphy, D.M., Farley, R.D., Purnell, I.J., Rowlands, C.C., Yacob, A.R., Paganini, M.C. and Giamello, E. (1999) *Journal of Physical Chemistry B*, **103**, 1944.

24 Chiesa, M., Paganini, M.C., Giamello, E., Di Valentin, C. and Pacchioni, G. (2003) *Angewandte Chemie–International Edition*, **42**, 1759.

25 Ricci, D., Di Valentin, C., Pacchioni, G., Sushko, P.V., Shluger, A.L. and Giamello, E. (2003) *Journal of the American Chemical Society*, **125**, 738.

26 Chiesa, M., Paganini, M.C., Spoto, G., Giamello, E., Di Valentin, C., Del Vitto, A. and Pacchioni, G. (2005) *Journal of Physical Chemistry B*, **109**, 7314.

27 Chiesa, M., Martino, P., Giamello, E., Di Valentin, C., Del Vitto, A. and Pacchioni, G. (2004) *Journal of Physical Chemistry B*, **108**, 11529.

28 Chiesa, M., Giamello, E., Annino, G., Massa, C.A. and Murphy, D.M. (2007) *Chemical Physics Letters*, **438**, 285.

29 Sterrer, M., Fischbach, E., Risse, T. and Freund, H.-J. (2005) *Physical Review Letters*, **94**, 186101.

30 Di Valentin, C., Neyman, K.M., Risse, T., Sterrer, M., Fischbach, E., Freund, H.-J., Pacchioni, G. and Rosch, N. (2006) *Journal of Chemical Physics*, **124**, 044708.

31 Sterrer, M., Fischbach, E., Heyde, M., Nilius, N., Rust, H-P, Risse, T. and Freund, H.-J. (2006) *Journal of Physical Chemistry B*, **110**, 8665.

32 Katter, U.J., Schlienz, H., Beckendorf, M. and Freund, H.-J. (1993) *Berichte Der Bunsen-Gesellschaft-Physical Chemistry Chemical Physics*, **97**, 340.

33 Katter, U.J., Risse, T., Schlienz, H., Beckendorf, M., Klüner, T., Hamann, H. and Freund, H.-J. (1997) *Journal of Magnetic Resonance*, **126**, 242.

34 Schmidt, J., Risse, T., Hamann, H. and Freund, H.-J. (2002) *Journal of Chemical Physics*, **116**, 10861.

35 Risse, T., Schmidt, J., Hamann, H. and Freund, H.-J. (2002) *Angewandte Chemie–International Edition*, **41**, 1517.

36 Sterrer, M., Yulikov, M., Fischbach, E., Heyde, M., Rust, H.-P., Paccioni, G., Risse, T. and Freund, H.-J. (2006) *Angewandte Chemie–International Edition*, **45**, 2630.

37 Yulikov, M., Sterrer, M., Heyde, M., Rust, H.-P., Risse, T., Freund, H.-J., Pacchioni, G. and Scagnelli, A. (2006) *Physical Review Letters*, **96**, 146804.

38 Lunsford, J.J. and Jayne, J.P. (1965) *Journal of Physical Chemistry*, **69**, 2182.

39 Teramura, K., Tanaka, T., Ishikawa, H., Kohono, Y. and Funabiki, T. (2004) *Journal of Physical Chemistry B*, **108**, 346.

40 Chiesa, M. and Giamello, E. (2007) *Chemistry–A European Journal*, **13**, 1261.

41 Che, M. and Tench, A.J. (1983) *Advances in Catalysis*, **32**, 1.

42 Che, M. and Tench, A.J. (1982) *Advances in Catalysis*, **31**, 77.

43 Giamello, E., Murphy, D.M., Marchese, L., Martra, G. and Zecchina, A. (1993) *Journal of the Chemical Society, Faraday Transactions*, **89**, 3715.

44 Chiesa, M., Giamello, E., Paganini, M.C. and Sojka, Z. (2002) *Journal of Chemical Physics*, **116**, 4266.

45 Ricci, D., Pacchioni, G., Sushko, P.V. and Shluger, A.L. (2003) *Surface Science*, **542**, 293.

46 Chiesa, M., Giamello, E., Murphy, D.M., Pacchioni, G., Paganini, M.C., Soave, R. and Sojka, Z. (2001) *Journal of Physical Chemistry B*, **105**, 497.

47 Gonzalez-Elipe, A.R. and Che, M. (1982) *Journal de Chimie Physique*, **79**, 355.

48 Attwood, A.L., Edwards, J.L., Rowlands, C.C. and Murphy, D.M. (2003) *Journal of Physical Chemistry A*, **107**, 1779.

49 Carter, E., Carley, A.F. and Murphy, D.M. (2007) *Journal of Chemical Physics and Physical Chemistry*, **8**, 113.

50 Jenkins, C.A. and Murphy, D.M. (1999) *Journal of Physical Chemistry B*, **103**, 1019.

51 Carter, E., Carley, A.F. and Murphy, D.M. (2007) *Journal of Physical Chemistry C*, **111**, 10630.

52 Labanowska, M. (2001) *Journal of Chemical Physics and Physical Chemistry*, **2**, 712.

53 Pietrzyk, P. and Sojka, Z. (2007) *Chemical Communications*, **1930**, 1930–1932.

54 Risse, T., Schmidt, J., Hamann, H. and Freund, H.-J. (2002) *Angewandte Chemie–International Edition*, **41**, 1517.

55 Schmidt, J., Risse, T., Hamann, H. and Freund, H.-J. (2002) *Journal of Chemical Physics*, **116**, 10861.

56 Neese, F. (2007) Quantum Chemical Approaches to Spin Hamiltonian Parameters, in *Electron Paramagnetic Resonance* (eds B.C. Gilbert, M.J. Davies and D.M. Murphy), Royal Society of Chemistry, Cambridge, **20**, p. 73.